

# Train Small, Model Big: Scalable Physics Simulators via Reduced Order Modeling and Domain Decomposition

Seung Whan Chung<sup>a,\*</sup>, Youngsoo Choi<sup>b</sup>, Pratanu Roy<sup>c</sup>, Thomas Moore<sup>d</sup>,  
Thomas Roy<sup>e</sup>, Tiras Y. Lin<sup>e</sup>, Du T. Nguyen<sup>a</sup>, Christopher Hahn<sup>f,g</sup>, Eric B.  
Duoss<sup>a,h</sup>, Sarah E. Baker<sup>f</sup>

<sup>a</sup>*Material Engineering Division, Lawrence Livermore National  
Laboratory, Livermore, 94550, CA, US*

<sup>b</sup>*Center for Applied Scientific Computing, Lawrence Livermore National  
Laboratory, Livermore, 94550, CA, US*

<sup>c</sup>*Atmospheric, Earth and Energy Division, Lawrence Livermore National  
Laboratory, Livermore, 94550, CA, US*

<sup>d</sup>*School of Mechanical, Medical and Process Engineering, Queensland University of  
Technology, Brisbane, 4000, QLD, Australia*

<sup>e</sup>*Computational Engineering Division, Lawrence Livermore National  
Laboratory, Livermore, 94550, CA, US*

<sup>f</sup>*Material Science Division, Lawrence Livermore National  
Laboratory, Livermore, 94550, CA, US*

<sup>g</sup>*Laboratory for Energy Applications for the Future, Lawrence Livermore National  
Laboratory, Livermore, 94550, CA, US*

<sup>h</sup>*Center for Engineered Materials, Manufacturing and Optimization, Lawrence Livermore  
National Laboratory, Livermore, 94550, CA, US*

---

## Abstract

Numerous cutting-edge scientific technologies originate at the laboratory scale, but transitioning them to practical industry applications is a formidable challenge. Traditional pilot projects at intermediate scales are costly and time-consuming. An alternative, the E-pilot, relies on high-fidelity numerical simulations, but even these simulations can be computationally prohibitive at larger scales. To overcome these limitations, we propose a scalable, physics-constrained reduced order model (ROM) method. ROM identifies critical physics modes from small-scale unit components, projecting governing equations onto these modes to create a reduced model that retains

---

\*corresponding author

*Email address:* chung28@llnl.gov (Seung Whan Chung)

essential physics details. We also employ Discontinuous Galerkin Domain Decomposition (DG-DD) to apply ROM to unit components and interfaces, enabling the construction of large-scale global systems without data at such large scales. This method is demonstrated on the Poisson and Stokes flow equations, showing that it can solve equations about 15–40 times faster with only  $\sim 1\%$  relative error. Furthermore, ROM takes one order of magnitude less memory than the full order model, enabling larger scale predictions at a given memory limitation.

*Keywords:* Reduced order model, E-pilot, Domain decomposition, Stokes flow, Poisson equation, Scalable physics simulator

---

## 1. Introduction

The scale-up of nascent technologies is a notoriously difficult task. While thousands of novel technologies are proposed in the academic literature each year, only a small fraction leave the laboratory and find commercial success. Among those that *do* succeed, the average time from conception to commercialization is as high as 35 years [1]. New industrial technologies typically require demonstration via a pilot plant, which often cost tens of millions of dollars and can take years to design, construct and operate. Given the urgent threat of climate change and the need for rapid decarbonization across the industrial sector, approaches for accelerating technology scale-up are desperately needed.

One promising approach is the development of “E-pilots”: fully resolved computational simulations that model industrial processes rigorously from first principles. High fidelity simulations can often be constructed via conventional numerical methods providing accurate predictions based on the underlying physics [2–5]. However, fully resolved three-dimensional simulations of multiphysics problems at industrial scales often prove numerically infeasible. As a concrete example, Singh *et al.* [6] developed a rigorous simulation of two-phase fluid flow within a novel packing material for carbon capture. While their simulations showed excellent agreement with experiment, they were expensive even at the laboratory scale: simulating 30 seconds of unsteady two-phase flow within a 15 cm tall reactor required 3 days on 144 cores. By way of comparison, Petra Nova’s industrial-scale CCS absorber [7] is roughly  $\sim 750\times$  taller and has about 10 million times more volume than the lab-scale system. Clearly, high-fidelity simulations of such systems are

numerically infeasible when conducted via standard methods.

Our goal in this work is to develop a reduced modeling framework that can provide sufficiently accurate, robust predictions at large scales in an efficient manner. It is worth taking a moment to expand on these goals. By *sufficiently accurate*, we mean simulations whose predictions match a rigorous numerical simulation to within a few percent relative error. Engineering parameters such as material properties or system geometry come with similar degrees of uncertainty, so further increasing mathematical accuracy beyond this point gives diminishing returns at the cost of increased computational time. By *robust*, we mean an ability to simulate over a wide range of parameters without catastrophic failure, and in particular the ability to accurately predict *emergent* properties that arise as the size of the system grows from the laboratory scale to industrial scales. For example, bench-scale reactors tend to be more isothermal (due to their relatively high specific surface area) while industrial scale reactors are more susceptible to large temperature changes, which can then impact reaction conversion and selectivities. A challenge in developing this framework is that if a system is too large to simulate via conventional methods, then, by definition, there is no numerical, system-scale data available with which to develop a data-based simulation approach. A successful, data-driven framework must instead be trained on data on smaller domains, and must then somehow extrapolate this training in a robust manner to larger scales where data are unavailable.

Data-driven machine learning techniques have been emerging as a promising alternative to the conventional physics simulations [8–10]. Relying on a large amount of experimental/simulation data, they attempt to replace the conventional physics simulation with a sparse dynamical system [8] or a neural network [9, 10]. However, these approaches have yet to be improved in their accuracy, particularly when the prediction is made outside the training data. More fundamentally, even with a well-trained model at a particular scale, it is not so clear how to extend it toward larger scales without any available data. Such extrapolation in scale is the major bottleneck in applying these data-driven methods directly as E-pilots.

Projection-based reduced order model (ROM) can be a promising alternative for this type of problem, taking the advantages of both the high-fidelity simulation and the data-driven approach. It effectively approximates the solution with the most dominant physics ‘modes’ as given by proper orthogonal decomposition (POD) of the solution sample data [11–18]. Typically the first 10  $\sim$  20 modes are sufficient to accurately represent the solution. By project-

ing the PDEs onto a subspace spanned by these critical modes, the number of unknowns can be reduced from thousands (as in a typical FEM discretization) to dozens. Then, significant acceleration can be achieved by neglecting the minor details. At the same time, ROMs can make robust extrapolative predictions as they are built upon the high-fidelity simulation models.

ROM has been widely used in many scientific and engineering applications, producing many variants. Among them, component ROMs exhibit remarkable capability in extending outcomes for large-scale systems based solely on data from smaller unit cells. These component ROMs have been successfully employed across a spectrum of physical problems, including lattice-type structure design optimization [19, 20], microtruss structures [21], heat conduction/exchange [22–24], linear elasticity [22], and acoustic Helmholtz problems [25]. However, it is important to note that the performance of these component approaches hinges on their ability to accurately represent interfaces with POD bases separate from the interior of the domain. This can add complexity to the decomposition and recomposition of domains with these component ROM methods.

To address this challenge, we propose a novel physics-constrained data-driven component ROM that offers both speed and accuracy in predicting outcomes for large-scale systems, all without the need to handle interfaces separately. To accomplish this, we leverage a discontinuous-Galerkin domain decomposition (DG-DD) approach [2, 26]. The component-level ROM begins by identifying the dominant modes within a given physics system based on component-level sample data. Subsequently, the governing equation at component level is projected onto the linear subspace defined by these identified modes, yielding a component-level ROM. DG-DD, on the other hand, decomposes a larger global system into smaller-scale components, where the component-level ROMs serve as foundational building blocks that are seamlessly integrated into the overarching global-scale ROM. In effect, we train our model on a small domain, and then compose many small domains together into a larger system. Because the underlying ROM still solves the governing physics equations (albeit on a small function space with an optimally-chosen basis) the methodology is robust to extrapolation, and in particular may be expected to capture ‘emergent phenomena’, such as large changes in temperature, not seen in the laboratory scale. This integrated approach allows for accurate and efficient predictions on a large scale, all while circumventing the need of handling interfaces and the interiors of domains separately.

There have been similar model reduction approaches that employ the

discontinuous Galerkin projection. For example, the discontinuous Galerkin reduced basis element method generates homogenous or particular solutions with parametrized forcing or boundary condition at subdomains, and formulates the discontinuous Galerkin projection with them as spectral basis [27, 28]. Their basis generation approach is distinctly different from our data-driven ROM, in that our ROM basis can be constructed from general samples, whether they are homogenous or particular, or a combination of both. Similarly, Yano [29] applied ROM with empirical quadrature points for DG discretization of nonlinear conservation laws. However, in this work the use of DG discretization is mainly to inherit the energy stability of the DG scheme, and the domain decomposition is not taken into account. Any of these works does not consider the potential of ROM and DG-DD for the robust and simple extrapolation in scale, while our proposed method does.

In this paper, we focus on general linear PDE systems, with the examples of the Poisson equation and the Stokes flow equation. Our framework could allow the possibility of extending to nonlinear systems, by being augmented with nonlinear ROM techniques such as the tensorial approach [30] and hyper-reduction [31–34].

The rest of the paper is organized as follows. In Section 2, the proposed component reduced-order modeling is formulated with respect to a general system of partial differential equations (PDE). Then Section 3 and 4 demonstrates the application of the general framework in Section 2 to the Poisson equation and the Stokes flow equation, respectively.

## 2. General framework

### 2.1. Physics governing equation and its domain decomposition

We consider a generic form of a linear governing equation for a physics system state  $\tilde{\mathbf{q}}$  on a two- or three-dimensional global domain  $\Omega$ ,

$$\mathcal{L}[\tilde{\mathbf{q}}] = \mathbf{f}, \tag{1}$$

where  $\mathcal{L}$  is the linear operator of  $\tilde{\mathbf{q}}$ . Unless otherwise stated, we consider a time-independent solution  $\tilde{\mathbf{q}} \in H^1(\Omega)^k$  with solution dimension  $k$ , and  $\mathbf{f} \in L_2(\Omega)^k$ . However, the proposed model reduction method can readily be extended to time-dependent problems as well.

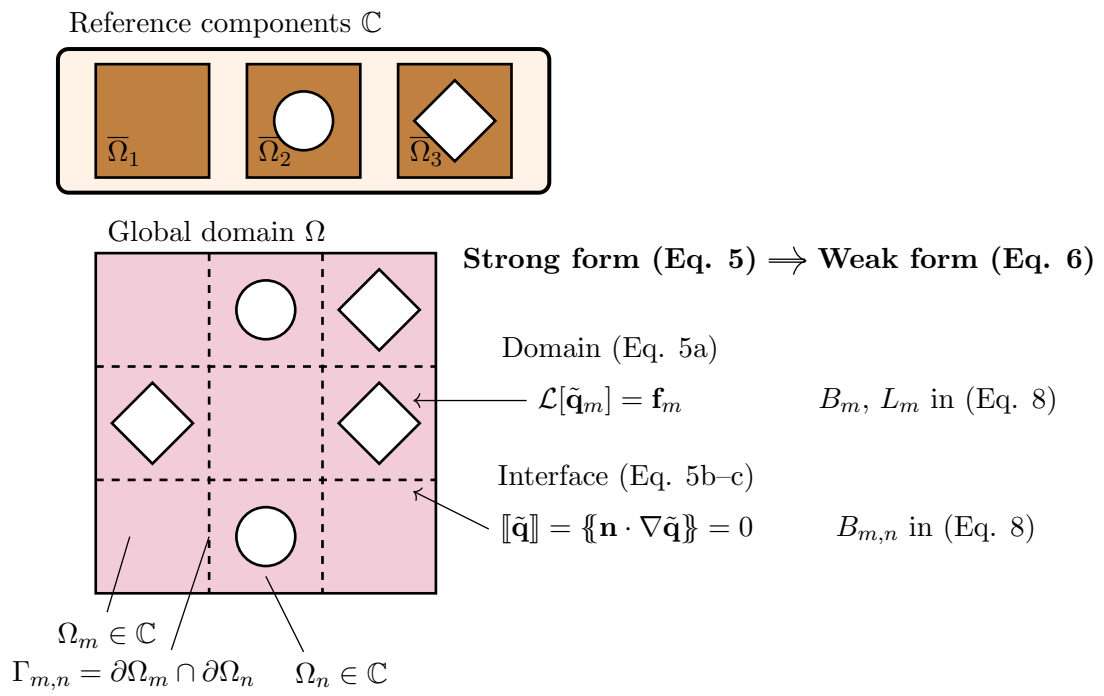


Figure 1: Illustration of domain decomposition.

We consider the global-scale domain  $\Omega$  decomposed into  $M$  subdomains  $\Omega_m$ ,

$$\Omega = \bigcup_{m=1}^M \Omega_m, \quad (2)$$

where all subdomains can be categorized into a few reference domains,

$$\Omega_m \in \mathbb{C} \equiv \{\bar{\Omega}_1, \bar{\Omega}_2, \dots\} \quad \forall m = 1, \dots, M. \quad (3)$$

The physics system state  $\tilde{\mathbf{q}}$  is composed of subdomain state  $\tilde{\mathbf{q}}_m \in H_1(\Omega_m)$ ,

$$\tilde{\mathbf{q}} = \{\tilde{\mathbf{q}}_m\}_{m=1}^M. \quad (4)$$

Each  $\tilde{\mathbf{q}}_m$  satisfies the governing equation on its subdomain,

$$\mathcal{L}[\tilde{\mathbf{q}}_m] = \mathbf{f}_m \quad \text{in } \Omega_m, \quad (5a)$$

with the continuity and smoothness constraints on the interface  $\Gamma_{m,n} \equiv \partial\Omega_m \cap \partial\Omega_n$ ,

$$[[\tilde{\mathbf{q}}]] \equiv \tilde{\mathbf{q}}_m - \tilde{\mathbf{q}}_n = 0 \quad \text{on } \Gamma_{m,n} \quad (5b)$$

$$\{\{\mathbf{n} \cdot \nabla \tilde{\mathbf{q}}\}\} \equiv \frac{1}{2} (\mathbf{n}_m \cdot \nabla \tilde{\mathbf{q}}_m + \mathbf{n}_n \cdot \nabla \tilde{\mathbf{q}}_n) = 0 \quad \text{on } \Gamma_{m,n}, \quad (5c)$$

where  $\mathbf{n}_m$  is the outward normal vector of the subdomain  $\Omega_m$ , and  $\mathbf{n}_m = -\mathbf{n}_n$  on  $\Gamma_{m,n}$ . Figure 1 illustrates (5) with an example of 3-by-3 global domain constructed with 3 types of components.

## 2.2. Discontinuous Galerkin (DG) domain decomposition

Standard Galerkin finite-element discretization seeks an approximate solution  $\mathbf{q} \in \mathbb{Q}_s$  that satisfies (1) in a weak sense,

$$B\langle \mathbf{q}^\dagger, \mathcal{L}[\mathbf{q}] \rangle = L\langle \mathbf{q}^\dagger, \mathbf{f} \rangle, \quad (6)$$

for all test function  $\mathbf{q}^\dagger \in \mathbb{Q}_s$ . The Dirichlet boundary condition will be weakly enforced via DG formulation.  $\mathbb{Q}_s \subset H^1(\Omega)$  is the piecewise  $s$ -th order polynomial function space composed of  $M$  subdomain finite element spaces,

$$\mathbb{Q}_s = \prod_{m=1}^M \mathbb{Q}_{m,s}. \quad (7)$$

The specific definition of  $\mathbb{Q}_{m,s}$  will be introduced in the applications in Section 3 and 4. The bilinear form  $B\langle \cdot, \cdot \rangle$  and the linear form  $L\langle \cdot, \cdot \rangle$  are the global-scale weak forms corresponding to the operators  $\mathcal{L}$ ,  $\mathcal{N}$  and the right-hand side  $\mathbf{f}$ , respectively.

We seek a weak form (6) that approximates (5) in place of (1), where each global-scale weak form is decomposed for subdomains and their interfaces. First, the bilinear form  $B\langle \cdot, \cdot \rangle$  is decomposed as

$$\begin{aligned} B\langle \mathbf{q}^\dagger, \mathcal{L}[\mathbf{q}] \rangle &= \sum_{m=1}^M B_m\langle \mathbf{q}^\dagger, \mathcal{L}[\mathbf{q}] \rangle + \sum_{(m,n) \in \mathbb{I}} B_{m,n}\langle \mathbf{q}^\dagger, \mathcal{L}[\mathbf{q}] \rangle \\ &+ \sum_{m=1}^M B_{m,di}\langle \mathbf{q}^\dagger, \mathbf{q} \rangle, \end{aligned} \quad (8a)$$

where  $B_m$  is the subdomain bilinear form defined on  $\Omega_m$ ,  $B_{m,n}$  is the interface bilinear form defined on all interfaces  $\Gamma_{m,n}$  with  $\mathbb{I} = \{(m, n) \mid \Gamma_{m,n} \neq \emptyset\}$ , and  $B_{m,di}$  is the Dirichlet boundary bilinear form defined on  $\Gamma_{m,di} \equiv \partial\Omega_m \cap \partial\Omega_{di}$ .

The linear form  $L\langle \cdot, \cdot \rangle$  is decomposed into subdomain linear forms  $L_m$  and the boundary linear forms,

$$L\langle \mathbf{q}^\dagger, \mathbf{f} \rangle = \sum_{m=1}^M L_m\langle \mathbf{q}^\dagger, \mathbf{f} \rangle + L_{ne}\langle \mathbf{q}^\dagger, \mathbf{f} \rangle + L_{di}\langle \mathbf{q}^\dagger, \mathbf{f} \rangle, \quad (8b)$$

where the Neumann boundary linear form  $L_{ne}$  is defined on  $\partial\Omega_{ne}$ , and the Dirichlet boundary linear form  $L_{di}$  on  $\partial\Omega_{di}$ . The specific definitions of these operators will be introduced in the applications in Section 3 and 4. Figure 1 illustrates how these weak-form operators in (8) correspond to the strong-form equation (5).

In DG domain decomposition [2, 26, 35], the interface operators in (8) act as a penalty against the violation of the interface constraints (5b–c), restricting the violation below discretization error. Thus, it enforces the interface constraints (5b–c) only weakly, without introducing Lagrange multiplier variables for the constraints as in other strongly enforced domain decomposition methods [36, 37]. This can be applied flexibly to general Galerkin methods: the subdomain operators  $B_m$  and  $L_m$  can be defined both in a continuous and in a discontinuous manner. If extending an existing finite-element solver, only the interface and boundary operators need to be implemented. Furthermore, such weak enforcement can also bring an advantage in model reduction. The reduced model significantly decreases the number of unknowns in

the system, making the strong interface enforcement a stringent constraint for such an overdetermined system, worsening the overall accuracy [38, 39]. Hoang *et al.* [38] reported that weakly constraining the interface condition improves the accuracy of the reduced model. While their weak enforcement is based on a random sampling, somewhat far from the physics, DG domain decomposition introduces the weak enforcement from the baseline governing equation, ensuring the violation remains within the discretization error.

These weak forms can also be written as matrix-vector inner products, which explicitly show the operators that will be projected onto the reduced linear subspace in the subsequent section. For bilinear operators,

$$B_m \langle \mathbf{q}^\dagger, \mathcal{L}[\mathbf{q}] \rangle = \mathbf{q}_m^{\dagger\top} \mathbf{B}_m \mathbf{q}_m \quad (9a)$$

$$B_{m,n} \langle \mathbf{q}^\dagger, \mathcal{L}[\mathbf{q}] \rangle = (\mathbf{q}_m^{\dagger\top} \quad \mathbf{q}_n^{\dagger\top}) \begin{pmatrix} \mathbf{B}_{mm} & \mathbf{B}_{mn} \\ \mathbf{B}_{nm} & \mathbf{B}_{nn} \end{pmatrix} \begin{pmatrix} \mathbf{q}_m \\ \mathbf{q}_n \end{pmatrix} \quad (9b)$$

$$B_{m,di} \langle \mathbf{q}^\dagger, \mathcal{L}[\mathbf{q}] \rangle = \mathbf{q}_m^{\dagger\top} \mathbf{B}_{m,di} \mathbf{q}_m, \quad (9c)$$

where  $\mathbf{B}_m, \mathbf{B}_{m,di} \in \mathbb{R}^{N_m \times N_m}$  with  $N_m \equiv \dim(\mathbf{q}_m)$  degrees of freedom for  $\mathbf{q}_m$ , and  $\mathbf{B}_{i,j} \in \mathbb{R}^{N_i \times N_j}$ . For linear form operators,

$$L_m \langle \mathbf{q}^\dagger, \mathbf{f} \rangle = \mathbf{q}_m^{\dagger\top} \mathbf{L}_m[\mathbf{f}] \quad (10a)$$

$$L_{ne} \langle \mathbf{q}^\dagger, \mathbf{f} \rangle = \mathbf{q}^{\dagger\top} \mathbf{L}_{ne}[\mathbf{f}] \quad (10b)$$

$$L_{di} \langle \mathbf{q}^\dagger, \mathbf{f} \rangle = \mathbf{q}^{\dagger\top} \mathbf{L}_{di}[\mathbf{f}], \quad (10c)$$

where  $\mathbf{L}_m : L_2(\Omega_m) \rightarrow \mathbb{R}^{N_m}$  and  $\mathbf{L}_{ne}, \mathbf{L}_{di} : L_2(\Omega) \rightarrow \mathbb{R}^N$  with  $N \equiv \dim \mathbf{q}$  degrees of freedom for the global solution  $\mathbf{q}$ .

The weak-form operators in (9–10) lay the groundwork for constructing reduced-order model components, which then can be assembled into a global scale reduced-order model. The construction and assembly procedure of the reduced-order model is described subsequently.

### 2.3. Linear subspace model reduction

Since all subdomains can be categorized into a few reference domains (3), we attempt to identify a linear subspace for each reference domain  $\bar{\Omega}_r$ , the basis for the reduced model component. All sample solutions for the decomposed system (5) are first categorized by their reference domains, constituting

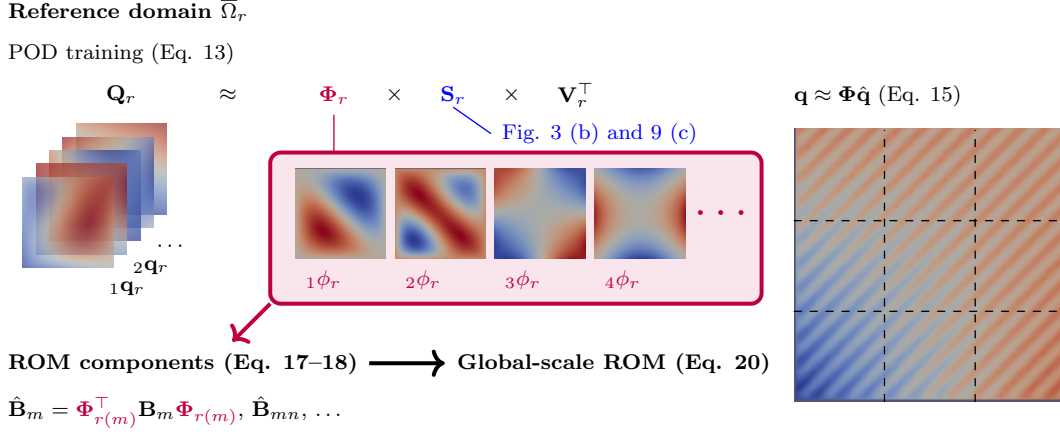


Figure 2: Diagram of the component reduced-order modeling procedure.

the corresponding snapshot matrix  $\mathbf{Q}_r \in \mathbb{R}^{N_r \times S_r}$ ,

$$\mathbf{Q}_r = \begin{pmatrix} | & | & | \\ 1\mathbf{q}_r & 2\mathbf{q}_r & \cdots \\ | & | & | \end{pmatrix}, \quad (11a)$$

where all sample solutions  ${}_i\mathbf{q}_r$  lie on the reference domain  $\bar{\Omega}_r$ , i.e.,

$$\text{dom}({}_i\mathbf{q}_r) = \bar{\Omega}_r \quad \forall i. \quad (11b)$$

Specific sampling procedures for generating  $\mathbf{Q}_r$  will be introduced in each application in Section 3 and 4. The well-known proper orthogonal decomposition (POD) is used to decompose  $\mathbf{Q}_r$  [40–42],

$$\begin{aligned} \mathbf{Q}_r &= \tilde{\Phi}_r \tilde{\mathbf{S}}_r \tilde{\mathbf{V}}_r^\top \\ &= \begin{pmatrix} | & | & | \\ 1\phi_r & 2\phi_r & \cdots \\ | & | & | \end{pmatrix} \begin{pmatrix} 1\sigma_r & & \\ & 2\sigma_r & \\ & & \cdots \end{pmatrix} \begin{pmatrix} \cdots \\ \cdots \\ \cdots \\ 1\mathbf{v}_r^\top \\ \cdots \\ 2\mathbf{v}_r^\top \\ \vdots \end{pmatrix}. \end{aligned} \quad (12)$$

The column vectors of  $\tilde{\Phi}_r$  correspond to the inherent physics modes we attempt to identify, spanning the linear space on which all the snapshots  ${}_i\mathbf{q}_r$  lie. The singular value  ${}_i\sigma_r$  indicates the average magnitude of the basis vector

${}_i\phi_r$  over all the snapshots in  $\mathbf{Q}_r$ . The right singular vector  ${}_i\mathbf{v}_r$  shows how the composition of  ${}_i\phi_r$  varies over each snapshot  ${}_i\mathbf{q}_r$ , which does not play a major role here.

The singular values  $\tilde{\mathbf{S}}_r$  provide meaningful information from the snapshot data for constructing the linear subspace. In essence, the singular value  ${}_i\sigma_r$  corresponds to the total energy of the mode  ${}_i\phi_r$  within the snapshot sample  $\mathbf{Q}_r$  [42]. In other words, the  ${}_i\phi_r$  with the larger  ${}_i\sigma_r$  corresponds to the most dominant physics modes representing the snapshots. In many applications, the singular values of a few major  ${}_i\phi_r$  can cover a significant portion of the norm of  $\mathbf{Q}_r$ , indicating that the snapshots in  $\mathbf{Q}_r$  can be well explained with only a few major modes. We therefore attempt to approximate  $\mathbf{Q}_r$  in the linear subspace of a reduced number, say  $R_r \ll S_r$ , of basis vectors  ${}_i\phi_r$ ,

$$\begin{aligned} \mathbf{Q}_r &\approx \Phi_r \mathbf{S}_r \mathbf{V}_r^\top \\ &= \left( \begin{array}{c|c|c} \vdots & \vdots & \vdots \\ \hline {}_1\phi_r & \cdots & {}_{R_r}\phi_r \\ \hline \vdots & & \vdots \end{array} \right) \begin{pmatrix} {}_1\sigma_r & & \\ & \cdots & \\ & & {}_{R_r}\sigma_r \end{pmatrix} \begin{pmatrix} \vdots \\ \hline {}_1\mathbf{v}_r^\top \\ \vdots \\ \hline {}_{R_r}\mathbf{v}_r^\top \\ \vdots \end{pmatrix}. \end{aligned} \quad (13)$$

Figure 2 illustrates this approximation with an example of the Poisson equation that will be demonstrated in Section 3. Any other solution we attempt to predict on  $\bar{\Omega}_r$  is also approximated by this reduced number of basis vectors,

$$\mathbf{q}_r \approx \Phi_r \hat{\mathbf{q}}_r. \quad (14)$$

The global-scale solution  $\mathbf{q}$  is approximated in each subdomain,

$$\mathbf{q} \approx \Phi \hat{\mathbf{q}} \equiv \begin{pmatrix} \Phi_{r(1)} & & & \\ & \cdots & & \\ & & \Phi_{r(m)} & \\ & & & \cdots \\ & & & & \Phi_{r(M)} \end{pmatrix} \begin{pmatrix} \hat{\mathbf{q}}_1 \\ \vdots \\ \hat{\mathbf{q}}_m \\ \vdots \\ \hat{\mathbf{q}}_M \end{pmatrix}, \quad (15)$$

where  $r(m)$  is the reference domain corresponding to the subdomain  $m$ .

We project the decomposed system (5) onto the linear subspaces of  $\Phi$ . In particular, we consider Galerkin projection where the test function is also approximated with the same linear subspace,

$$\mathbf{q}^\dagger \approx \Phi \hat{\mathbf{q}}^\dagger. \quad (16)$$

The matrix operators of the bilinear form in (9) are then reduced to

$$\begin{aligned} B_m \langle \mathbf{q}^\dagger, \mathcal{L}[\mathbf{q}] \rangle &\approx \hat{B}_m \langle \hat{\mathbf{q}}^\dagger, \hat{\mathbf{q}} \rangle \\ &\equiv \hat{\mathbf{q}}_m^{\dagger\top} \hat{\mathbf{B}}_m \hat{\mathbf{q}}_m \equiv \hat{\mathbf{q}}_m^{\dagger\top} (\Phi_{r(m)}^\top \mathbf{B}_m \Phi_{r(m)}) \hat{\mathbf{q}}_m \end{aligned} \quad (17a)$$

$$\begin{aligned} B_{m,n} \langle \mathbf{q}^\dagger, \mathcal{L}[\mathbf{q}] \rangle &\approx \hat{B}_{m,n} \langle \hat{\mathbf{q}}^\dagger, \hat{\mathbf{q}} \rangle \\ &\equiv (\hat{\mathbf{q}}_m^{\dagger\top} \quad \hat{\mathbf{q}}_n^{\dagger\top}) \begin{pmatrix} \hat{\mathbf{B}}_{mm} & \hat{\mathbf{B}}_{mn} \\ \hat{\mathbf{B}}_{nm} & \hat{\mathbf{B}}_{nn} \end{pmatrix} \begin{pmatrix} \hat{\mathbf{q}}_m \\ \hat{\mathbf{q}}_n \end{pmatrix} \\ &\equiv (\hat{\mathbf{q}}_m^{\dagger\top} \quad \hat{\mathbf{q}}_n^{\dagger\top}) \begin{pmatrix} \Phi_{r(m)}^\top \mathbf{B}_{mm} \Phi_{r(m)} & \Phi_{r(m)}^\top \mathbf{B}_{mn} \Phi_{r(n)} \\ \Phi_{r(n)}^\top \mathbf{B}_{nm} \Phi_{r(m)} & \Phi_{r(n)}^\top \mathbf{B}_{nn} \Phi_{r(n)} \end{pmatrix} \begin{pmatrix} \hat{\mathbf{q}}_m \\ \hat{\mathbf{q}}_n \end{pmatrix} \end{aligned} \quad (17b)$$

$$\begin{aligned} B_{m,d} \langle \mathbf{q}^\dagger, \mathcal{L}[\mathbf{q}] \rangle &\approx \hat{B}_{m,d} \langle \hat{\mathbf{q}}^\dagger, \hat{\mathbf{q}} \rangle \\ &\equiv \hat{\mathbf{q}}_m^{\dagger\top} \hat{\mathbf{B}}_{m,d} \hat{\mathbf{q}}_m \equiv \hat{\mathbf{q}}_m^{\dagger\top} (\Phi_{r(m)}^\top \mathbf{B}_{m,d} \Phi_{r(m)}) \hat{\mathbf{q}}_m. \end{aligned} \quad (17c)$$

Likewise, the vectors of the linear form in (10) are also reduced to

$$\begin{aligned} L_m \langle \mathbf{q}^\dagger, \mathbf{f} \rangle &\approx \hat{L}_m \langle \hat{\mathbf{q}}^\dagger, \mathbf{f} \rangle \\ &\equiv \hat{\mathbf{q}}_m^{\dagger\top} \hat{\mathbf{L}}_m [\mathbf{f}] \equiv \hat{\mathbf{q}}_m^{\dagger\top} (\Phi_{r(m)}^\top \mathbf{L}_m [\mathbf{f}]) \end{aligned} \quad (18a)$$

$$\begin{aligned} L_n \langle \mathbf{q}^\dagger, \mathbf{f} \rangle &\approx \hat{L}_n \langle \hat{\mathbf{q}}^\dagger, \mathbf{f} \rangle \\ &\equiv \hat{\mathbf{q}}^{\dagger\top} \hat{\mathbf{L}}_n [\mathbf{f}] \equiv \hat{\mathbf{q}}^{\dagger\top} (\Phi^\top \mathbf{L}_n [\mathbf{f}]) \end{aligned} \quad (18b)$$

$$\begin{aligned} L_d \langle \mathbf{q}^\dagger, \mathbf{f} \rangle &\approx \hat{L}_d \langle \hat{\mathbf{q}}^\dagger, \mathbf{f} \rangle \\ &\equiv \hat{\mathbf{q}}^{\dagger\top} \hat{\mathbf{L}}_d [\mathbf{f}] \equiv \hat{\mathbf{q}}^{\dagger\top} (\Phi^\top \mathbf{L}_d [\mathbf{f}]). \end{aligned} \quad (18c)$$

(17–18) are the ROM components, which are assembled into the global-scale reduced-model operators analogous to (8),

$$\hat{B} \langle \hat{\mathbf{q}}^\dagger, \hat{\mathbf{q}} \rangle = \sum_{m=1}^M \hat{B}_m \langle \hat{\mathbf{q}}^\dagger, \hat{\mathbf{q}} \rangle + \sum_{(m,n) \in \mathbb{I}} \hat{B}_{m,n} \langle \hat{\mathbf{q}}^\dagger, \hat{\mathbf{q}} \rangle + \sum_{m=1}^M \hat{B}_{m,d} \langle \hat{\mathbf{q}}^\dagger, \hat{\mathbf{q}} \rangle \quad (19a)$$

$$\hat{L} \langle \hat{\mathbf{q}}^\dagger, \mathbf{f} \rangle = \sum_{m=1}^M \hat{L}_m \langle \hat{\mathbf{q}}^\dagger, \mathbf{f} \rangle + \hat{L}_n \langle \hat{\mathbf{q}}^\dagger, \mathbf{f} \rangle + \hat{L}_d \langle \hat{\mathbf{q}}^\dagger, \mathbf{f} \rangle. \quad (19b)$$

The global-scale reduced model analogous to (6) is

$$\hat{B} \langle \hat{\mathbf{q}}^\dagger, \hat{\mathbf{q}} \rangle = \hat{L} \langle \hat{\mathbf{q}}^\dagger, \mathbf{f} \rangle, \quad (20)$$

which is solved for  $\hat{\mathbf{q}}$  with respect to all  $\hat{\mathbf{q}}^\dagger$ . Figure 2 illustrates the procedure of global-scale ROM construction.

It is worth emphasizing that the global-scale full-order model (6) need not be solved at all for constructing the reduced model (20). Neither does it need to be constructed at all, throughout the entire reduced model construction. The entire procedure can be executed only at the reference component domain level. The snapshots in  $\mathbf{Q}_r$  (11) can be obtained by solving (6) only on  $\bar{\Omega}_r$  with appropriate  $\mathbf{f}$  and boundary conditions. The reduced basis  $\Phi_r$  is then calculated only from this component-scale snapshots. Any subdomain can be categorized with a reference domain per (3), so it is possible to pre-compute the reduced operators in (19) with respect to the reference domains and their interfaces. For example,  $\hat{B}_m \langle \hat{\mathbf{q}}^\dagger, \hat{\mathbf{q}} \rangle$  in (17a) can use the pre-computed operator  $\hat{\mathbf{B}}_{r(m)}$ ,

$$\hat{B}_m \langle \hat{\mathbf{q}}^\dagger, \hat{\mathbf{q}} \rangle = \hat{\mathbf{q}}_m^{\dagger\top} \hat{\mathbf{B}}_{r(m)} \hat{\mathbf{q}}_m \equiv \hat{\mathbf{q}}_m^{\dagger\top} (\Phi_{r(m)}^\top \mathbf{B}_{r(m)} \Phi_{r(m)}) \hat{\mathbf{q}}_m, \quad (21)$$

where  $\mathbf{B}_{r(m)}$  can be constructed with the reference domain  $\bar{\Omega}_r$  only. Likewise, the interface operator  $\hat{B}_{r,r'}$  in (17b) can be precomputed for an interface between  $\bar{\Omega}_r$  and  $\bar{\Omega}_{r'}$ , and used for all  $(m, n)$  with  $r(m) = r$  and  $r(n) = r'$ .

### 3. Poisson equation

#### 3.1. Governing equation

For  $\tilde{\mathbf{q}} \equiv \tilde{u} \in H^1(\Omega)$ ,  $\mathbf{f} \equiv f \in L_2(\Omega)$ , the governing equation (1) for the Poisson equation is

$$-\nabla^2 \tilde{u} = f \quad \text{in } \Omega, \quad (22a)$$

with boundary conditions on  $\partial\Omega = \partial\Omega_{di} \cup \partial\Omega_{ne}$ ,

$$\tilde{u} = g_{di} \quad \text{on } \partial\Omega_{di}, \quad (22b)$$

$$\mathbf{n} \cdot \nabla \tilde{u} = g_{ne} \quad \text{on } \partial\Omega_{ne}. \quad (22c)$$

(22) is decomposed into subdomains as in (5),

$$-\nabla^2 \tilde{u}_m = f \quad \text{in } \Omega_m \quad (23a)$$

with interface constraints on  $\Gamma_{m,n}$ ,

$$[[\tilde{u}]] = 0, \quad (23b)$$

$$\{\{\mathbf{n} \cdot \nabla \tilde{u}\}\} = 0. \quad (23c)$$

### 3.2. Weak form finite element formulation

For the interface handling we follow the formulation of Hansbo [26], though other DG-type domain decomposition techniques can be used as well. Our choice of the finite element space (7) is

$$\mathbb{Q}_{m,s} = \left\{ u_m \in H^1(\Omega_m) \mid u_m|_{\kappa} \in V_s(\kappa) \quad \forall \kappa \in \mathcal{T}(\Omega_m) \right\}, \quad (24)$$

where  $\mathcal{T}(\Omega_m)$  is the set of mesh elements in subdomain  $\Omega_m$ , and  $V_s(\kappa)$  is the space of  $s$ th-order polynomials in a mesh element  $\kappa$ . Under this choice, the FE formulation of each subdomain remains continuous Galerkin, enforcing only the interface constraints in a discontinuous Galerkin way. However, another choice is also available where the entire system is formulated as a DG FE discretization.

The weak form of (23) corresponding to (6) is formulated with respect to  $\mathbf{q}^\dagger = \{u_m^\dagger\}$  and  $\mathbf{q} = \{u_m\}$ . The weak-form operators in (8) are defined as

$$B_m \langle \mathbf{q}^\dagger, \mathcal{L}[\mathbf{q}] \rangle = \langle \nabla u_m^\dagger, \nabla u_m \rangle_{\Omega_m}, \quad (25a)$$

$$\begin{aligned} B_{m,n} \langle \mathbf{q}^\dagger, \mathcal{L}[\mathbf{q}] \rangle = & - \langle \{\{\mathbf{n} \cdot \nabla u^\dagger\}\}, \llbracket u \rrbracket \rangle_{\Gamma_{m,n}} - \langle \llbracket u^\dagger \rrbracket, \{\{\mathbf{n} \cdot \nabla u\}\} \rangle_{\Gamma_{m,n}} \\ & + \langle \gamma \Delta \mathbf{x}^{-1} \llbracket u^\dagger \rrbracket, \llbracket u \rrbracket \rangle_{\Gamma_{m,n}}, \end{aligned} \quad (25b)$$

with  $\Delta \mathbf{x}$  the diameter of the elements and  $\gamma > 0$  the penalty strength for interface constraints. On the Dirichlet boundary of the subdomain  $\Gamma_{m,di} = \partial\Omega_m \cap \partial\Omega_{di}$ ,

$$\begin{aligned} B_{m,di} \langle \mathbf{q}^\dagger, \mathbf{q} \rangle = & - \langle \mathbf{n} \cdot \nabla u^\dagger, u \rangle_{\Gamma_{m,di}} - \langle u^\dagger, \mathbf{n} \cdot \nabla u \rangle_{\Gamma_{m,di}} \\ & + \langle \gamma \Delta \mathbf{x}^{-1} u^\dagger, u \rangle_{\Gamma_{m,di}}. \end{aligned} \quad (25c)$$

The linear weak-form operators are defined as

$$L_m \langle \mathbf{q}^\dagger, \mathbf{f} \rangle = \langle u_m^\dagger, f \rangle_{\Omega_m}, \quad (26a)$$

$$L_{ne} \langle \mathbf{q}^\dagger, \mathbf{f} \rangle = \langle u^\dagger, g_{ne} \rangle_{\partial\Omega_{ne}}, \quad (26b)$$

$$L_{di} \langle \mathbf{q}^\dagger, \mathbf{f} \rangle = \langle u^\dagger, \gamma \Delta \mathbf{x}^{-1} g_{di} \rangle_{\partial\Omega_{di}} + \langle \mathbf{n} \cdot \nabla u^\dagger, g_{di} \rangle_{\partial\Omega_{di}}. \quad (26c)$$

The resulting weak form discretized system is positive definite for a sufficiently large  $\gamma$  [26], where  $\gamma = (s+1)^2$  is used for  $\mathbf{q} \equiv u \in \mathbf{Q}_s$  in our application [43]. The full order model (FOM) discretization (5) is implemented for (23) in the MFEM framework, which is an open-source C++ library for finite element methods [43].

### 3.3. Component-level samples for linear subspace training

In this demonstration, we consider a single component of a two-dimensional unit square domain  $\mathbb{C} = \{\bar{\Omega}_1\}$ ,  $\bar{\Omega}_1 = [0, 1]^2$ . The domain  $\bar{\Omega}_1$  is discretized into a mesh with  $64^2$  uniform rectangular elements. We consider  $s = 1$ , i.e. first-order polynomial function space for  $\mathbb{Q}_{m,s}$  (24), leading to  $N_1 = 4225$  degrees of freedom for the FOM in  $\bar{\Omega}_1$ .

For sample generation, the right-hand side is defined in a general sinusoidal form with parameters  $\mathbf{k} \in \mathbb{R}^2$  and  $\theta \in \mathbb{R}$ ,

$$f = \sin 2\pi(\mathbf{k} \cdot \mathbf{x} + \theta). \quad (27a)$$

The entire boundary is set as a Dirichlet condition, i.e.  $\partial\bar{\Omega}_1 \equiv \partial\bar{\Omega}_{1,di}$ , with parameters  $\mathbf{k}_b \in \mathbb{R}^2$  and  $\theta_b \in \mathbb{R}$ ,

$$g_{di} = \sin 2\pi(\mathbf{k}_b \cdot \mathbf{x} + \theta_b). \quad (27b)$$

The parameter values of  $\mathbf{k}$ ,  $\mathbf{k}_b$ ,  $\theta$  and  $\theta_b$  are randomly chosen for each sample, thereby collecting a broad spectrum of solutions.  $\mathbf{k}$  and  $\mathbf{k}_b$  are chosen from a uniform random distribution of two-dimensional vectors,

$$\mathbf{k}, \mathbf{k}_b \in U[-0.5, 0.5]^2, \quad (28a)$$

and  $\theta$  and  $\theta_b$  are chosen from a scalar uniform random distribution,

$$\theta, \theta_b \in U[0, 1]. \quad (28b)$$

Figure 3(a) shows a sample solution with randomly chosen parameter values. In total,  $S_1 = 4225$  samples are collected for the snapshot matrix  $\mathbf{Q}_1$ . From  $\mathbf{Q}_1$ , the linear subspace basis vectors are identified via POD (12), under the `libROM` framework, which is an open-source library for ROM [44]. Figure 3(b) shows the singular values  $\text{diag}(\tilde{\mathbf{S}}_1)$  associated with the identified POD basis  $\tilde{\Phi}_1$ . The singular value spectrum decays rapidly, and 99.77% of the energy norm of the snapshot matrix is covered by only the first 15 basis vectors, i.e.

$$\sum_{i=1}^{15} \sigma_i \approx 0.9977 \sum_{s=1}^{S_1} \|\mathbf{q}_s\|. \quad (29)$$

From this we can expect that any test case can be effectively spanned by these first 15 basis vectors, unless it is significantly different from these snapshots. In practice, even the qualitatively different case can be robustly predicted with the component ROM constructed from this snapshot. This will be shown in the subsequent demonstration.

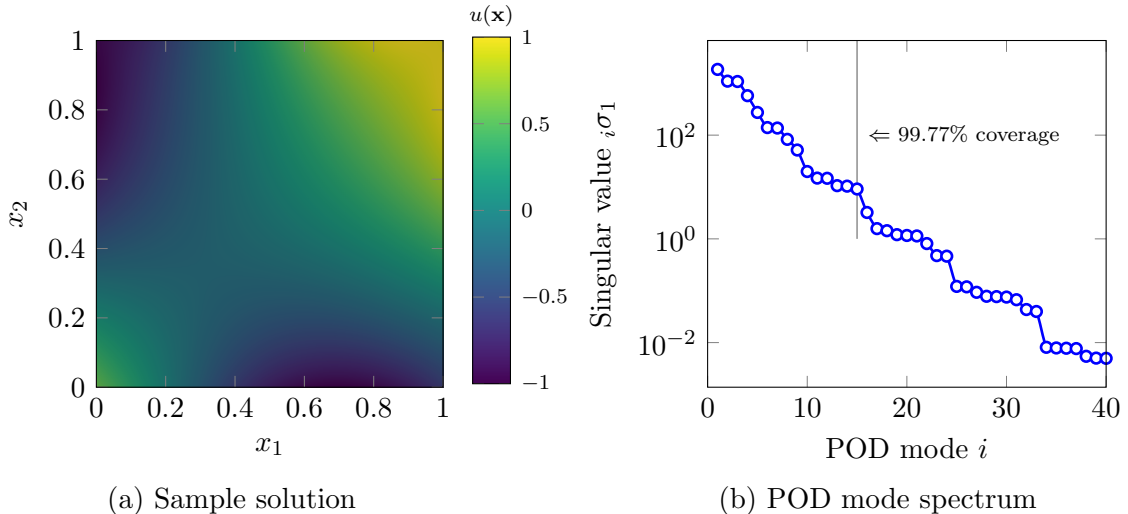


Figure 3: Sample generation and linear subspace training for the Poisson equation: (a) a sample solution in the component domain  $\bar{\Omega}_1$  with  $\mathbf{k} = (0.4, -0.3)$ ,  $\mathbf{k}_b = (0.5, 0.4)$ ,  $\theta = 0.1$  and  $\theta_b = 0.4$ ; and (b) Singular value spectrum of POD basis identified from  $\mathbf{Q}_1$ . The gray line indicates the 15-th singular value, up to which 99.77% of spectrum is covered.

### 3.4. Prediction performance

The ROM component (17–18) for the component  $\bar{\Omega}_1$  is built by projecting the component operator (25) and (26) onto the basis  $\Phi_1$ , which is obtained as described in Section 3.3. With the resulting ROM component, the global ROM (20) is then constructed per (19) at various sizes of the global domain, and tested for various right-hand sides  $f$  of (22).

In the following computational experiments, the comparison between FOM and ROM is made on an Intel Xeon CPU, running on a single thread with 3 GB of RAM and 2.1 GHz clock speed [45].

#### 3.4.1. Global-level prediction

The global ROM (20) for Poisson equation (22) is first demonstrated for the component problem (27), which was also used to generate the component-level samples. Six different sizes of the global domain are considered:  $\Omega = [0, 2^n]^2 \subset \mathbb{R}^2$  with  $M = n^2$  components of  $\bar{\Omega}_1$  for  $n = 2, 3, \dots, 7$ . For each size of the global domain, in order to investigate the robustness of prediction outside the training range, 100 test values of the parameters  $\{\mathbf{k}, \mathbf{k}_b, \theta, \theta_b\}$  are

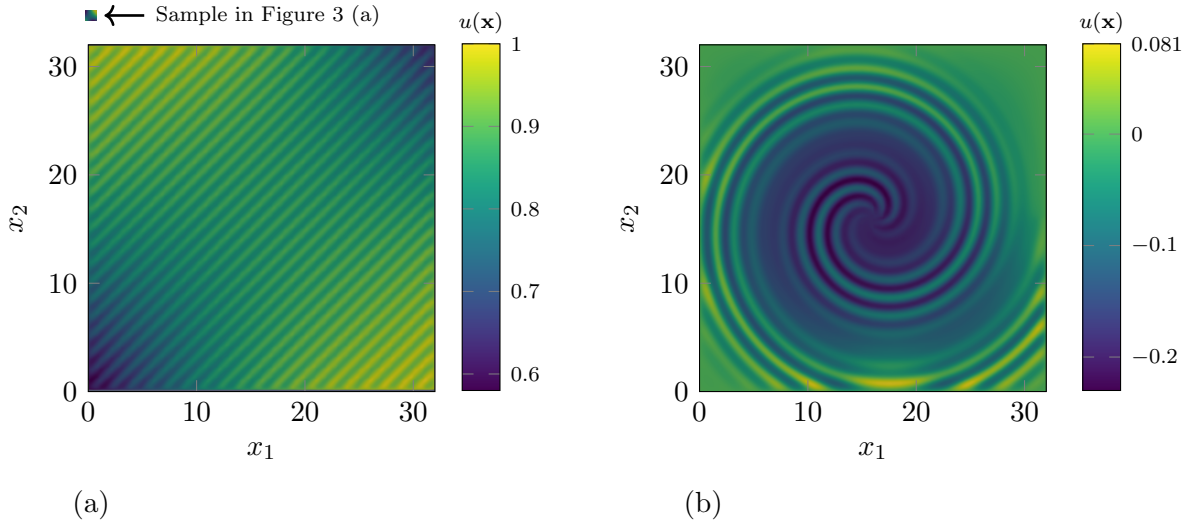


Figure 4: Example predictions on the global domain  $\Omega = [0, 32]^2$  with the global ROM (20) constructed with  $32^2$  components: ROM solutions for (a) the component problem (27) with  $\mathbf{k} = (0.6, -0.6)$ ,  $\mathbf{k}_b = (0.05, 0.04)$ ,  $\theta = 0.1$  and  $\theta_b = 0$ ; and for (b) the Spiral problem (32) with  $(s, k) = (1.53, 3)$ . The component-level sample from Figure 3 is included as a reference to compare size.

chosen from a range larger than the training data (28),

$$\mathbf{k}, \mathbf{k}_b \in [-0.7, 0.7]^2 \quad (30a)$$

$$\theta, \theta_b \in [0, 1]^2. \quad (30b)$$

Figure 4 (a) shows an example test prediction on the global domain of size  $[0, 32]^2$ .

Figure 5 shows the comparison between the FOM and the global ROM, depending on the size of the global domain. Here, both systems are solved using MUMPS, which is a direct LU-factorization linear solver [46, 47]. In Figure 5 (a), assembly time for both FOM and ROM system scales super-linearly with the number of components. The ROM global system does not need the assembly of the FOM global system, since the ROM operators are pre-computed per each reference as described in Section 2.3 (Eq. 21). Furthermore, the size of ROM operators ( $\mathbb{R}^{15 \times 15}$ ) is significantly smaller than that of FOM operators ( $\mathbb{R}^{4225 \times 4225}$ ), leading to a huge reduction of assembly time. For  $M > 32^2$ , the FOM system could not be assembled due to the

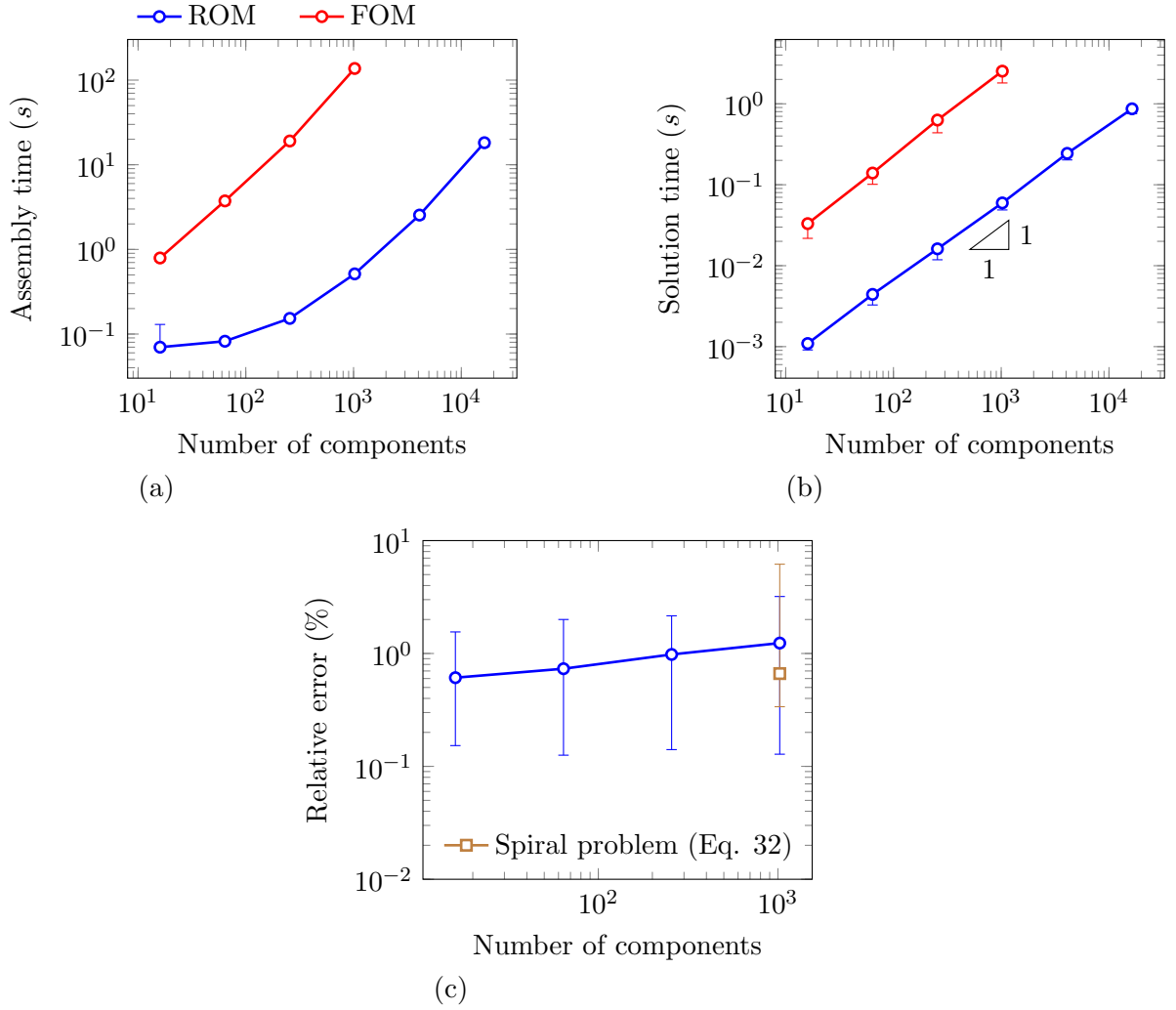


Figure 5: Performance of the ROM compared to the FOM for the Poisson equation, depending on the size of the domain: (a) assembly time of the system; (b) computation time of the system; and (c) relative error of the ROM compared to the FOM solution. The marker denotes the median value of 100 test cases, and the error bar denotes 95%-confidence interval of the test cases. Both ROM and FOM systems are solved using the conjugate-gradient method without any preconditioner.

memory limitations. On the other hand, the ROM system can be assembled for the larger domains under the same memory limitations, which is confirmed up to an  $M = 128^2$ -component domain. Except for a few outliers, the assembly times of both FOM and ROM are consistent over all 100 test cases.

Figure 5 (b) compares the computation time of solving the ROM and FOM systems. Compared to the FOM, the ROM accelerates the computation time about 30 times faster at  $M = 16$ . The speed-up factor increases up to 40 with the number of components, up to  $M = 1024$ . This speed-up trend was consistent over all 100 test cases, without any outlier. Meanwhile, the prediction accuracy of the ROM does not degrade regardless of the domain size. Figure 5 (c) shows the relative error of the ROM compared to the FOM solution,

$$\epsilon = \left[ \frac{\sum_m^M \|\mathbf{q}_m - \Phi_{r(m)} \hat{\mathbf{q}}_m\|_{\Omega_m}^2}{\sum_m^M \|\mathbf{q}_m\|_{\Omega_m}^2} \right]^{1/2}. \quad (31)$$

Throughout all cases, the relative error of the ROM solution remains at about 1%. While the accuracy of the ROM varies over the test cases, its variance is not so large: the largest variance was observed for  $M = 32^2$ -component domain, from 0.8% to 3%. This comparison clearly shows that the component ROM can effectively make a fast and robust prediction at an extrapolated scale.

We further demonstrate the robustness of the component ROM, with a test problem that is qualitatively different from the one used for the sample generation. We devised a right-hand side that has a sinusoidal wave along an Archimedean spiral for a domain  $\Omega = [0, L]^2$ ,

$$f = \exp\left(-\frac{|r - \frac{s\theta L}{4\pi}|^2}{2w^2}\right) \cos 2\pi k \left| r - \frac{s\theta L}{4\pi} \right|, \quad (32a)$$

where  $(r, \theta)$  are the polar coordinates of  $\mathbf{x}$  with respect to the center of  $\Omega$ ,

$$\begin{aligned} r &= |\mathbf{x} - (0.5L, 0.5L)| \\ \theta &= \tan^{-1} \frac{x_2 - 0.5L}{x_1 - 0.5L}. \end{aligned} \quad (32b)$$

The entire boundary is set with the homogeneous Dirichlet condition,

$$g_{di} = 0, \quad (32c)$$

with  $\partial\Omega \equiv \partial\Omega_{di}$ . Figure 4 (b) shows an example ROM solution of the spiral problem (32) on the global domain with  $L = 32$ . Such a spiral pattern was never seen from the samples, so the solution must be extrapolated out of the basis constructed from the samples of the linear wave problem (27). The same ROM system is tested for this spiral problem (32) over 100 test cases of parameter  $(s, k)$  within a range of

$$s \in U[0, 0.7] \quad k \in U[0, 0.7], \quad (33)$$

with  $L = 32$  and  $w = 2$ . Even for this qualitatively different case, the ROM was able to make robust predictions over all test cases. In Figure 5 (c), the ROM error for the spiral problem case remains  $\sim 0.7\%$  similar to the linear wave problem (27), varying from 0.2% to 6%.

#### 3.4.2. Performance with iterative solver

The use of a direct solver for a linear system is reasonable when the size of the system is not extremely large ( $\dim(\mathbf{q}) \gtrsim 10^7$ ) or when an optimal preconditioner is not well-established yet. In this work, we consider general PDE systems, for which preconditioning strategies are not necessarily assumed to be well-developed, so the direct solver is considered as the default linear system solver.

However, as the problem size increases, the direct method's cost can be intractable in both memory and computation time. This issue may also apply to ROM, although ROM tends to be less constrained by these limitations than FOM due to its reduced size. In such cases, the selection of a preconditioner for ROM becomes crucial in achieving optimal performance and should be given as much attention as the preconditioner for FOM. While the direct solver is perfectly suitable for our demonstration, we present the performance of an iterative solver for both FOM and ROM to illustrate how it scales with problem size. This comparison envisions the potential necessity for an optimal preconditioner for ROM.

Figure 6 shows the computation time for the ROM and the FOM system using the iterative conjugate gradient method. As the iterative solver does not require an LU factorization of the system like the direct method, the assembly time in Figure 6 (a) was shorter than the direct method in Figure 5 (b), for both FOM and ROM. However, this overhead cost for the direct method does not scale as fast as the matrix assembly itself, so its portion in the assembly time decreases with the problem size.

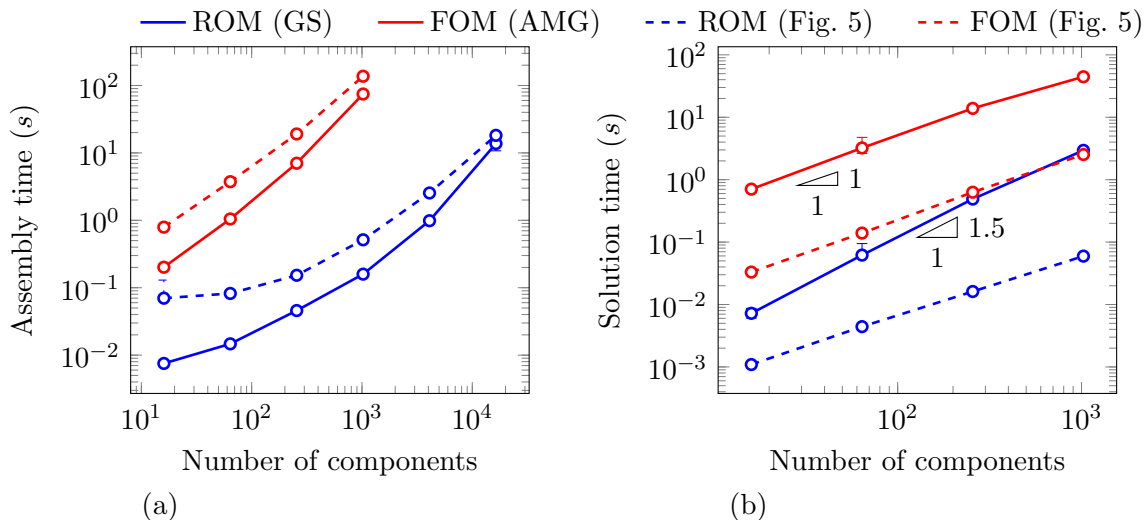


Figure 6: The comparison of (a) the assembly time and (b) the computation times between the ROM and the FOM for the Poisson component problem (27), using the conjugate gradient method with preconditioners (AMG for the FOM, and GS for the ROM). The marker denotes the median value of 100 test cases, and the error bar denotes 95%-confidence interval of the test cases. The results from Figure 5 are included as dashed lines for a reference to compare.

Figure 6 (b) shows the computation time for the ROM and the FOM system, both using a preconditioner. For the Poisson equation, various preconditioners have been developed, among which multi-grid methods have shown their supremacy over all others, in particular algebraic multi-grid (AMG) [48, 49]. This is indeed the case for our FOM system as well. For the FOM systems, though more expensive than the direct method, AMG efficiently solves the system with the complexity of  $\mathcal{O}(M)$ . The same AMG, however, does not necessarily accelerate the ROM system. Using other conventional preconditioners, such as symmetric Gauss-Seidel (GS) method, slightly improves the computation time, solving 100 times faster than the FOM with the AMG preconditioner. However, the scaling behavior remains  $\mathcal{O}(M^{1.5})$ , and the computation time gap between FOM and ROM decreases with the problem size. Although the ROM still solves the problem about 20 times faster than the FOM at our largest test case, its advantage over FOM decreases with the problem size.

The results in Figure 6 show a need for developing preconditioners for the ROM system. One main reason for the ineffectiveness of the conventional preconditioners on the ROM system is the sparse-block matrix structure of the ROM system: the system (20) is constructed with sparse non-zero block matrices, where each block matrix is dense based on the ROM operators (17). This is qualitatively different from what the conventional preconditioners are designed for.

A caveat in developing a preconditioner is that the effectiveness of a preconditioner is often problem-dependent. In many cases, an optimal preconditioner for a given PDE system is not simple to implement or well-established throughout the community. It also often involves prior physics knowledge for the given system to develop an optimal preconditioner [50–52], which is not always available. In such cases, the direct method is still a viable choice over a wide range of the problem size. This is even more so for ROM with its greatly reduced system size. Our goal in this research is to present a reduced order modeling approach for general PDE problems. Therefore, we did not further explore the options of developing an effective preconditioner for each problem, which is beyond the scope of our study.

### 3.4.3. Performance scaling with the number of basis

We further investigate the performance of the ROM depending on basis dimension  $R_1$ . For demonstration, the Poisson component problem (27) is solved for  $\Omega = [0, 4]^2$  with  $M = 4^2$  components, at a fixed parameter value

$$\mathbf{k} = (0.6, -0.6) \quad \mathbf{k}_b = (0.05, 0.04) \quad \theta = 0.1 \quad \theta_b = 0. \quad (34)$$

Figure 7(a) shows the computation time of the resulting ROM system, depending on basis dimension. The ROM system is solved via the same direct LU method. The computation time scales linearly as  $\mathcal{O}(R_1)$ . Due to this scaling, the ROM becomes as slow as the FOM only with a 200 basis dimension, however, its accuracy also scales rapidly with  $R_1$ . In Figure 7(b), the ROM already achieves below 1% error only with 16 basis vectors. Furthermore, the relative error of the ROM solution decays as  $\mathcal{O}(R_1^{-5})$ , much faster than the computation time. Considering that the ROM typically targets for a moderate accuracy of 0.1%  $\sim$  1%, this result implies that the proposed component ROM can achieve the desired accuracy only with the first few basis vectors.

While  $R_1 > 100$  would be beyond the practical range for ROM, we further investigated the scaling behavior to provide an insight about the linear-

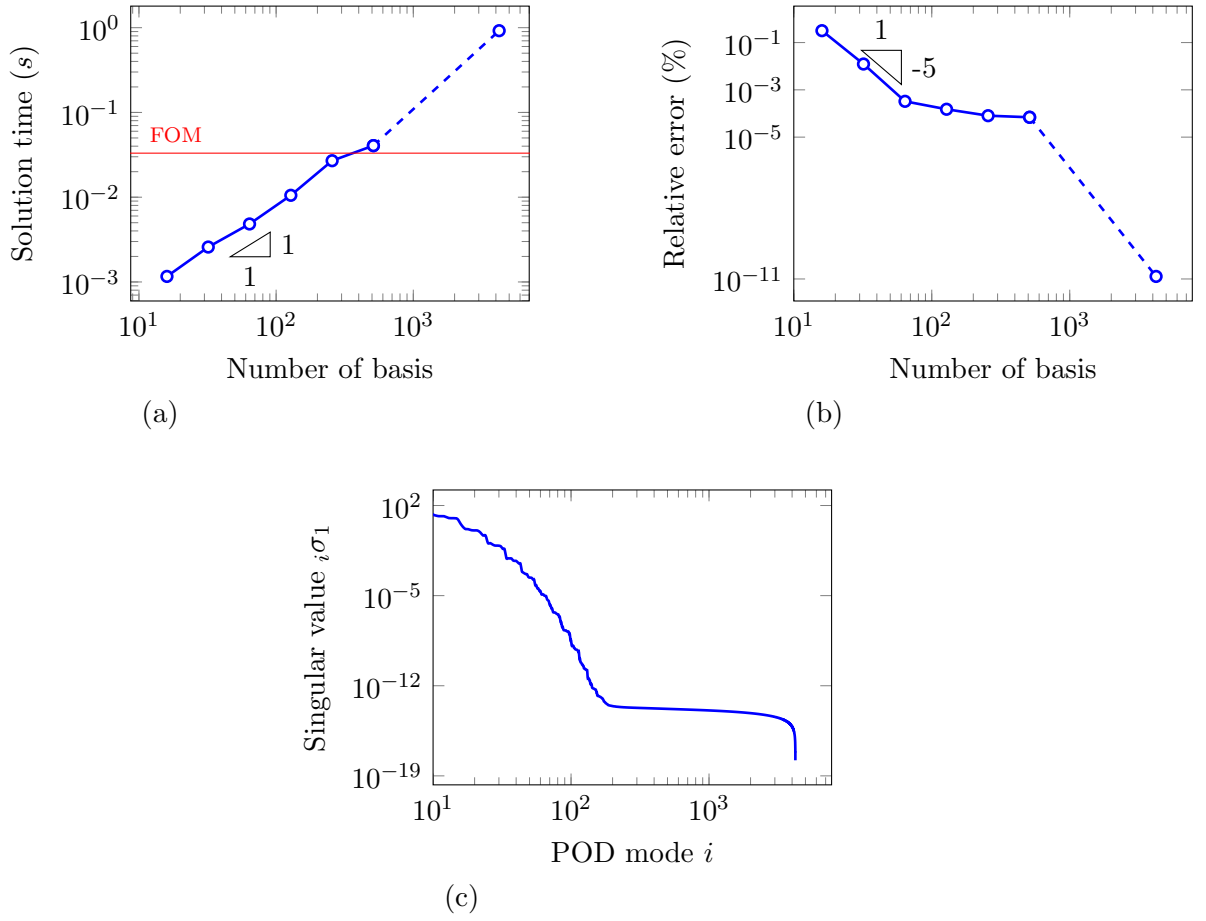


Figure 7: Performance scaling of the ROM with respect to the basis dimension  $R_1$ : (a) the computation time of the resulting ROM system; (b) the relative error of the ROM solution; and (c) the full spectrum of the singular values of the POD basis  $\Omega_1$  in Figure 3(b). The computation time for the FOM system is included as a reference to compare.

subspace ROM and sample generation. In Figure 7(b), the relative error seems to stagnate around  $10^{-4}\%$  for  $R_1 > 10^2$ . While there seems to be a constant factor of error, this is in fact related to how the linear subspace  $\Phi$  is identified. Figure 7(c) shows the full spectrum of the singular values of the POD basis  $\tilde{\Phi}_1$ . The singular values decrease rapidly down to a negligible value of  $10^{-12}$  around the 200th basis vector, indicating that the sample snapshot  $\mathbf{Q}_1$  can be perfectly spanned only with the first 200 POD basis vectors. The rest of the basis (about 4000 basis vectors) is essentially random orthonormal vectors corresponding to the null space of the snapshot  $\mathbf{Q}_1$ , which are not necessarily well factorized to represent the solution. When the prediction is outside the training data, a non-negligible portion of the solution may not be spanned by the first 200 basis vectors, where then the remaining 4000 basis vectors are used to represent this portion. However, since these 4000 basis vectors are not well factorized, this non-negligible portion requires essentially the entire basis in order to be effectively represented. This is confirmed in Figure 7 (b) by checking the accuracy of the ROM with  $R_1 = 4225 \equiv N_1$ . The relative error, which was seemingly stagnated previously, decreases down to a negligible value of  $10^{-12}$ .

This behavior shows an implicit impact of the samples on the resulting ROM performance. The richer the samples we collect for identifying the linear subspace, the broader the spectrum of the effective basis becomes, and therefore, the smaller error the ROM can achieve as it increases the basis dimension.

## 4. Stokes flow equation

### 4.1. Governing equation

The governing equation (1) for Stokes flow is defined for  $\tilde{\mathbf{q}} \equiv (\tilde{\mathbf{u}}, \tilde{p})$  with  $\tilde{\mathbf{u}} \in H^1(\Omega)^{\dim(\Omega)}$ ,  $\tilde{p} \in H^1(\Omega)$  and  $\mathbf{f} \equiv 0$ ,

$$-\nu \nabla^2 \tilde{\mathbf{u}} + \nabla \tilde{p} = 0 \quad \text{in } \Omega, \quad (35a)$$

$$\nabla \cdot \tilde{\mathbf{u}} = 0 \quad \text{in } \Omega, \quad (35b)$$

with boundary conditions on  $\partial\Omega$ ,

$$\tilde{\mathbf{u}} = \mathbf{g}_{di} \quad \text{on } \partial\Omega_{di}, \quad (35c)$$

$$\mathbf{n} \cdot (-\nu \nabla \tilde{\mathbf{u}} + \tilde{p} \mathbf{I}) = \mathbf{g}_{ne} \quad \text{on } \partial\Omega_{ne}, \quad (35d)$$

where  $\mathbf{u}$  and  $p$  denotes the velocity and pressure field respectively, and  $\nu \equiv \frac{\mu}{\mu_0} = 1.1$  is the non-dimensionalized dynamic viscosity with respect to a reference value. (35) describes the conservation of momentum with incompressibility condition. (35) is decomposed into subdomains as in (5),

$$-\nu \nabla^2 \tilde{\mathbf{u}}_m + \nabla \tilde{p}_m = 0 \quad \text{in } \Omega_m, \quad (36a)$$

$$\nabla \cdot \tilde{\mathbf{u}}_m = 0 \quad \text{in } \Omega_m, \quad (36b)$$

with interface constraints on  $\Gamma_{m,n}$ ,

$$[[\tilde{\mathbf{u}}]] = \{\{\mathbf{n} \cdot \nabla \tilde{\mathbf{u}}\}\} = 0, \quad (36c)$$

$$[[\tilde{p}]] = \{\{\mathbf{n} \cdot \nabla \tilde{p}\}\} = 0. \quad (36d)$$

#### 4.2. Weak form finite element formulation

Several choices of DG finite element spaces for Stokes flow are available for our domain decomposition framework [2, 3, 51]. Our choice of the finite element space (7) is Taylor-Hood elements [53],

$$\mathbf{q}_m \equiv (\mathbf{u}_m, p_m) \in \mathbb{Q}_{m,s} = \mathbb{U}_{m,s+1} \otimes \mathbb{P}_{m,s}, \quad (37a)$$

where the finite element spaces for velocity and pressure are defined respectively,

$$\mathbb{U}_{m,s} = \left\{ \mathbf{u}_m \in H^1(\Omega_m) \mid \mathbf{u}_m|_{\kappa} \in V_s(\kappa)^{\dim(\Omega)} \quad \forall \kappa \in \mathcal{T}(\Omega_m) \right\} \quad (37b)$$

$$\mathbb{P}_{m,s} = \left\{ p_m \in H^1(\Omega_m) \cap H_0^1(\Omega) \mid p_m|_{\kappa} \in V_s(\kappa) \quad \forall \kappa \in \mathcal{T}(\Omega_m) \right\}, \quad (37c)$$

where  $\mathbf{q}_m$  is discretized in a continuous Galerkin way as for the Poisson equation in Section 3. In (37a), the velocity space is defined one-order higher than the pressure space in order to satisfy the Ladyzhenskaya-Babuška-Brezzi (LBB) condition for existence of a solution [53–56]. In the case of  $\partial\Omega_{ne} = \emptyset$ , the pressure is restricted to have mean value zero in the global domain  $\Omega$ .

The weak form of (36) corresponding to (6) is formulated with respect to  $\mathbf{q}^\dagger = \{(\mathbf{u}_m^\dagger, p_m^\dagger)\}$  and  $\mathbf{q} = \{(\mathbf{u}_m, p_m)\}$ . The bilinear-form operators in (8) are defined as a block matrix form,

$$B_m \langle \mathbf{q}^\dagger, \mathcal{L}[\mathbf{q}] \rangle = \begin{pmatrix} a \langle \mathbf{u}^\dagger, \mathbf{u} \rangle_m & b \langle \mathbf{u}^\dagger, p \rangle_m \\ b \langle \mathbf{u}, p^\dagger \rangle_m & 0 \end{pmatrix}, \quad (38a)$$

where each block corresponds to

$$a\langle \mathbf{u}^\dagger, \mathbf{u} \rangle_m = \langle \nu \nabla \mathbf{u}_m^\dagger, \nabla \mathbf{u}_m \rangle_{\Omega_m} \quad (38b)$$

$$b\langle \mathbf{u}^\dagger, p \rangle_m = - \langle \nabla \cdot \mathbf{u}_m^\dagger, p_m \rangle_{\Omega_m}. \quad (38c)$$

Likewise, the interface bilinear weak form operator is

$$B_{m,n}\langle \mathbf{q}^\dagger, \mathcal{L}[\mathbf{q}] \rangle = \begin{pmatrix} a\langle \mathbf{u}^\dagger, \mathbf{u} \rangle_{m,n} & b\langle \mathbf{u}^\dagger, p \rangle_{m,n} \\ b\langle \mathbf{u}, p^\dagger \rangle_{m,n} & 0 \end{pmatrix}, \quad (38d)$$

with its blocks

$$\begin{aligned} a\langle \mathbf{u}^\dagger, \mathbf{u} \rangle_{m,n} &= - \langle \{ \mathbf{n} \cdot \nu \nabla \mathbf{u}^\dagger \}, [\mathbf{u}] \rangle_{\Gamma_{m,n}} \\ &\quad - \langle [\mathbf{u}^\dagger], \{ \mathbf{n} \cdot \nu \nabla \mathbf{u} \} \rangle_{\Gamma_{m,n}} \\ &\quad + \langle \gamma \Delta \mathbf{x}^{-1} [\mathbf{u}^\dagger], [\mathbf{u}] \rangle_{\Gamma_{m,n}} \end{aligned} \quad (38e)$$

$$b\langle \mathbf{u}^\dagger, p \rangle_{m,n} = \langle [\mathbf{n} \cdot \mathbf{u}^\dagger], \{ p \} \rangle_{\Gamma_{m,n}}. \quad (38f)$$

The boundary bilinear form on  $\Gamma_{m,di}$  the Dirichlet boundary of the subdomain is

$$B_{m,di}\langle \mathbf{q}^\dagger, \mathcal{L}[\mathbf{q}] \rangle = \begin{pmatrix} a\langle \mathbf{u}^\dagger, \mathbf{u} \rangle_{m,di} & b\langle \mathbf{u}^\dagger, p \rangle_{m,di} \\ b\langle \mathbf{u}, p^\dagger \rangle_{m,di} & 0 \end{pmatrix}, \quad (38g)$$

with its blocks

$$\begin{aligned} a\langle \mathbf{u}^\dagger, \mathbf{u} \rangle_{m,di} &= - \langle \mathbf{n} \cdot \nu \nabla \mathbf{u}^\dagger, \mathbf{u} \rangle_{\Gamma_{m,di}} \\ &\quad - \langle \mathbf{u}^\dagger, \mathbf{n} \cdot \nu \nabla \mathbf{u} \rangle_{\Gamma_{m,di}} \\ &\quad + \langle \gamma \Delta \mathbf{x}^{-1} \mathbf{u}^\dagger, \mathbf{u} \rangle_{\Gamma_{m,di}} \end{aligned} \quad (38h)$$

$$b\langle \mathbf{u}^\dagger, p \rangle_{m,di} = \langle \mathbf{n} \cdot \mathbf{u}^\dagger, p \rangle_{\Gamma_{m,di}}. \quad (38i)$$

With  $L_m\langle \mathbf{q}^\dagger, \mathbf{f} \rangle = 0$ , we only have the boundary linear weak form operators,

$$L_{ne}\langle \mathbf{q}^\dagger, \mathbf{f} \rangle = \begin{pmatrix} \langle \mathbf{u}^\dagger, \mathbf{g}_{ne} \rangle_{\partial\Omega_{ne}} \\ 0 \end{pmatrix} \quad (39a)$$

$$L_{di}\langle \mathbf{q}^\dagger, \mathbf{f} \rangle = \begin{pmatrix} \langle \mathbf{u}^\dagger, \gamma \Delta \mathbf{x}^{-1} \mathbf{g}_{di} \rangle_{\partial\Omega_{di}} + \langle \mathbf{n} \cdot \nu \nabla \mathbf{u}^\dagger, \mathbf{g}_{di} \rangle_{\partial\Omega_{di}} \\ \langle p^\dagger, \mathbf{n} \cdot \mathbf{g}_{di} \rangle_{\partial\Omega_{di}} \end{pmatrix} \quad (39b)$$

The interface penalty strength  $\gamma = \nu(s+1)^2$  is used for  $\mathbb{Q}_{m,s}$  to ensure the stability of the solution [2].

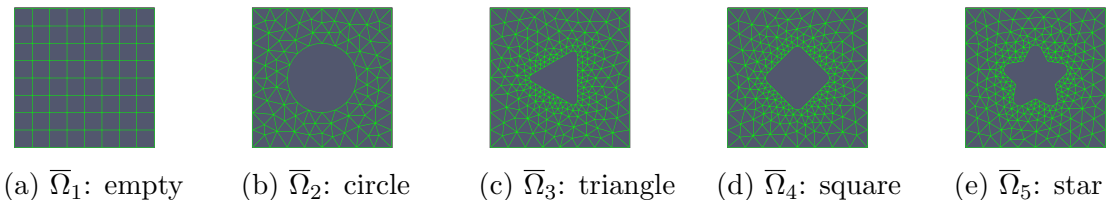


Figure 8: Reference domains used as components: (a) empty, (b) circle, (c) triangle, (d) square, and (e) star.

#### 4.3. Component-level samples for linear subspace training

For this demonstration, five different reference domains  $\mathbb{C} = \{\bar{\Omega}_1, \dots, \bar{\Omega}_5\}$  are considered as components for building up the global-scale system. All reference domains lie within a unit square  $\bar{\Omega}_r \subset [0, 1]^2$ , with an obstacle (or none) within them, as shown in Figure 8. The type and number of elements of each component is summarized in Table 1.

$\bar{\Omega}_r$ (name)	Element type	Number of elements	$N_r$	$S_r$
$\bar{\Omega}_1$ (empty)	quadrilateral	64	1539	1115
$\bar{\Omega}_2$ (circle)	triangular	168	2040	1076
$\bar{\Omega}_3$ (triangle)	triangular	393	4583	1098
$\bar{\Omega}_4$ (square)	triangular	372	4364	1114
$\bar{\Omega}_5$ (star)	triangular	415	4873	1197

Table 1: Specification of component reference domains.

Sample snapshots for basis training are generated on 2-by-2-component domains  ${}_s\Omega$  for  $s = 1, 2, \dots, 1400$ . For the  $s$ -th sample,  ${}_s\Omega = \bigcup_{m=1}^4 {}_s\Omega_m$  are constructed with four randomly chosen subdomains  ${}_s\Omega_m$  from  $\mathbb{C}$ . Figure 9(a) and 9(b) show two example sample domains. On each sample domain  ${}_s\Omega$ , a random inflow velocity is set with a sinusoidal perturbation for the Dirichlet boundary condition,

$$\mathbf{g}_{di} = (g_1 + \Delta g_1 \sin 2\pi(\mathbf{k}_1 \cdot \mathbf{x} + \theta_1), g_2 + \Delta g_2 \sin 2\pi(\mathbf{k}_2 \cdot \mathbf{x} + \theta_2)), \quad (40a)$$

on the Dirichlet boundary  ${}_s\partial\Omega_{di}$ , which represents the upwind sides of  ${}_s\Omega$ . At the surface of the object inside the domain, a no-slip wall boundary is set,

$$\mathbf{g}_{di} = \mathbf{0} \quad \text{on } {}_s\partial\Omega_0 \equiv \{\mathbf{x} \in {}_s\partial\Omega \mid x_1, x_2 \neq 0, 2\}. \quad (40b)$$

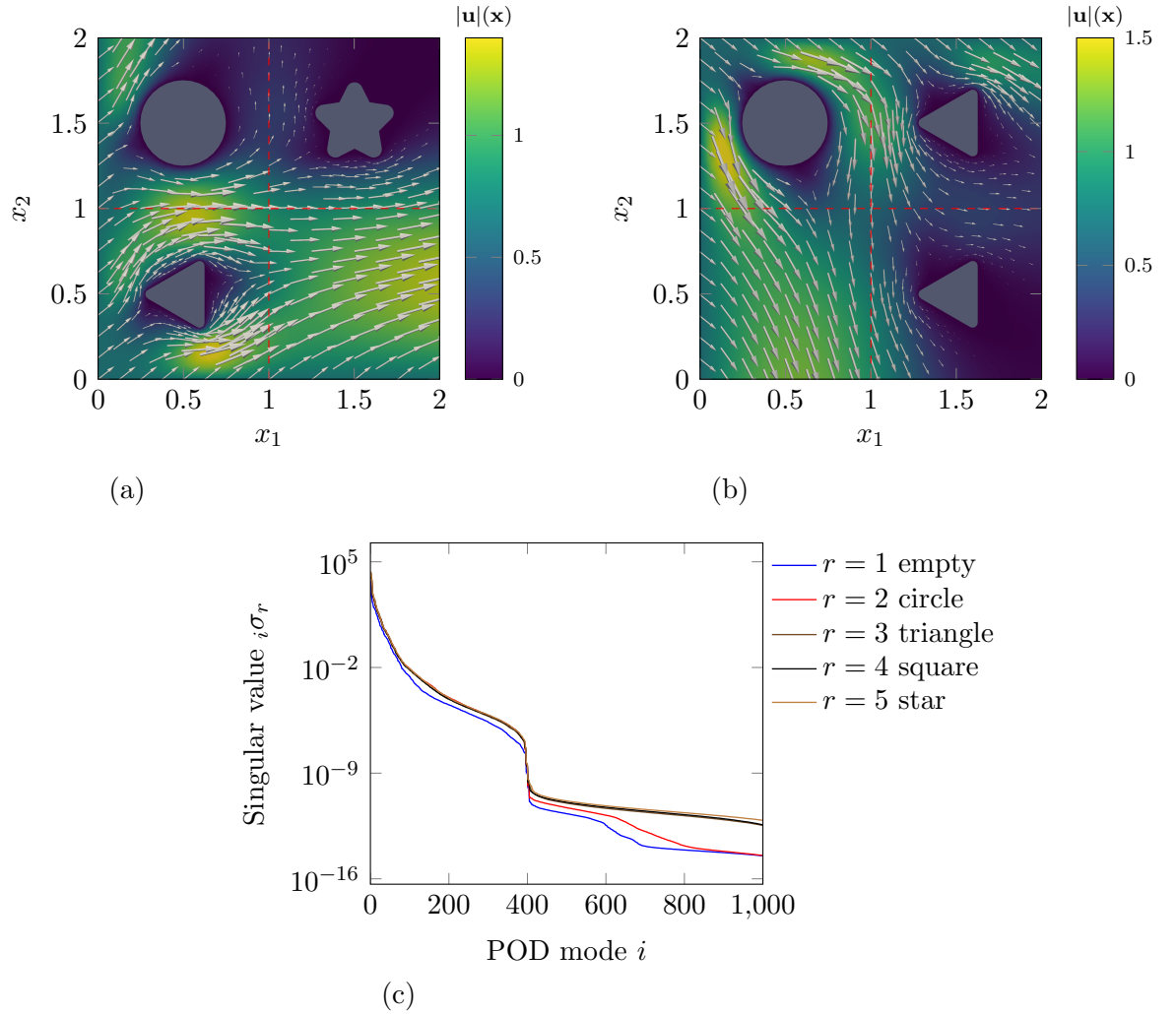


Figure 9: POD basis training for Stokes flow: an example sample domain and solution for the flow-past-array problem (40), with parameter values of (a)  $(g_1, g_2) = (0.5, 0.4)$  and (b)  $(g_1, g_2) = (0.5, -0.4)$ ; and (c) the singular value spectra of the trained POD basis for the reference domains. The arrows indicate the flow velocity  $\mathbf{u}$ .

The rest of the boundary is set as homogeneous Neumann boundary for  ${}_s\partial\Omega_{ne} = {}_s\partial\Omega/({}_s\partial\Omega_{di} \cup {}_s\partial\Omega_0)$ ,

$$\mathbf{g}_{ne} = \mathbf{0} \quad \text{on } {}_s\partial\Omega_{ne}. \quad (40c)$$

Figure 9 (a) and (b) show two example solutions from this flow-past-array problem (40). The sample inflow velocity is chosen from a uniform distribution,

$$g_1, g_2 \in U[-1, 1] \quad (41a)$$

$$\Delta g_1, \Delta g_2 \in U[-0.1, 0.1] \quad (41b)$$

$$\mathbf{k}_1, \mathbf{k}_2 \in U[-0.5, 0.5]^2 \quad (41c)$$

$$\theta_1, \theta_2 \in U[0, 1]. \quad (41d)$$

Table 1 shows the summary of the number of sample snapshots collected on each reference domain. Figure 9(c) shows the singular value spectra of POD modes trained on the reference domains.

In the trained POD modes, the velocity and pressure are coupled together. In other words, the POD basis  $\Phi_r$  for the reference domain  $r$  has the size of  $(N_r, R_r)$  with  $N_r = \dim(\mathbf{u}_r) + \dim(p_r)$ , and its basis vectors represent the modes of  $\mathbf{q}_r = (\mathbf{u}_r, p_r)$  as a whole. The resulting ROM (20) is then composed of  $M^2$  matrix blocks, where its  $(m, n)$  block matrix has the size of  $(R_{r(m)}, R_{r(n)})$ .

#### 4.4. Prediction performance

##### 4.4.1. Global-level prediction

We demonstrate the performance of the ROM with the same sample boundary condition (40), but on global domain  $\Omega(N_c) \subset [0, N_c]^2$  filled with  $N_c^2$  random components. The inflow velocity  $\mathbf{g}_{di}$  for (40) is chosen from an extended uniform distribution for 100 test cases at each size of the domain,

$$(g_1, g_2) \in U[-1.5, 1.5]^2. \quad (42)$$

Figure 10(a) shows the prediction made by ROM on a  $\Omega(32)$ .

The ROM constructed for the Stokes flow was capable of robust extrapolation in all scales, similar to the Poisson equation shown in Section 3. Figure 11 (c) shows the relative error of the ROM over 100 test cases at each size of the domain, which remains between 0.3% to 2%. Unlike for the

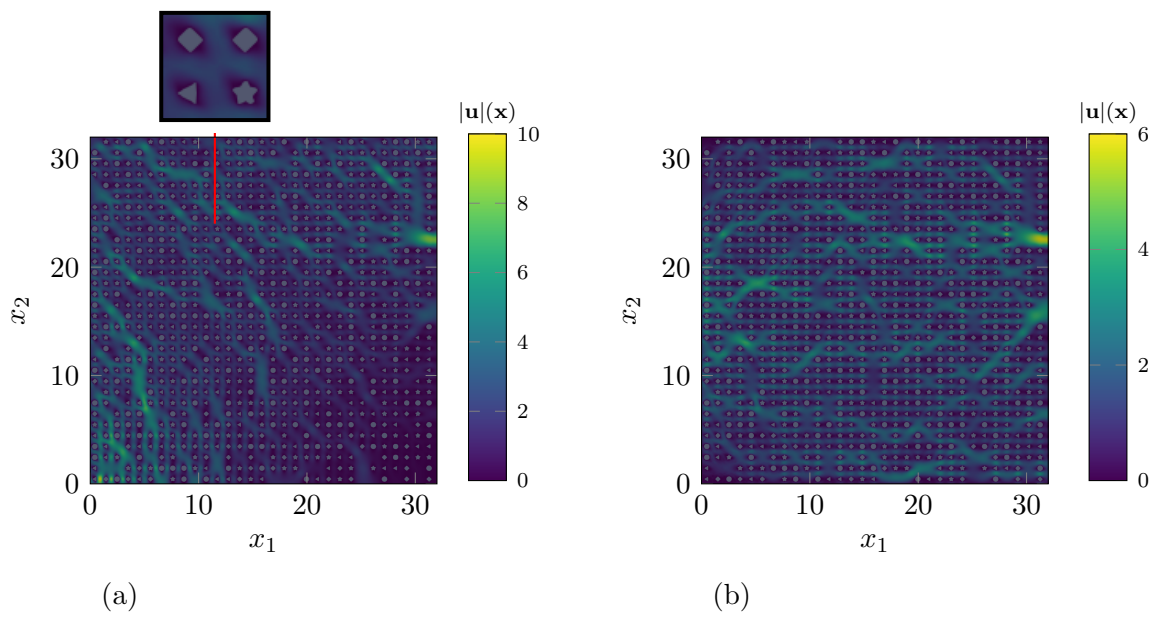


Figure 10: Test ROM predictions on  $\Omega(32)$ : (a) flow past array (40); and (b) channel flow (43).

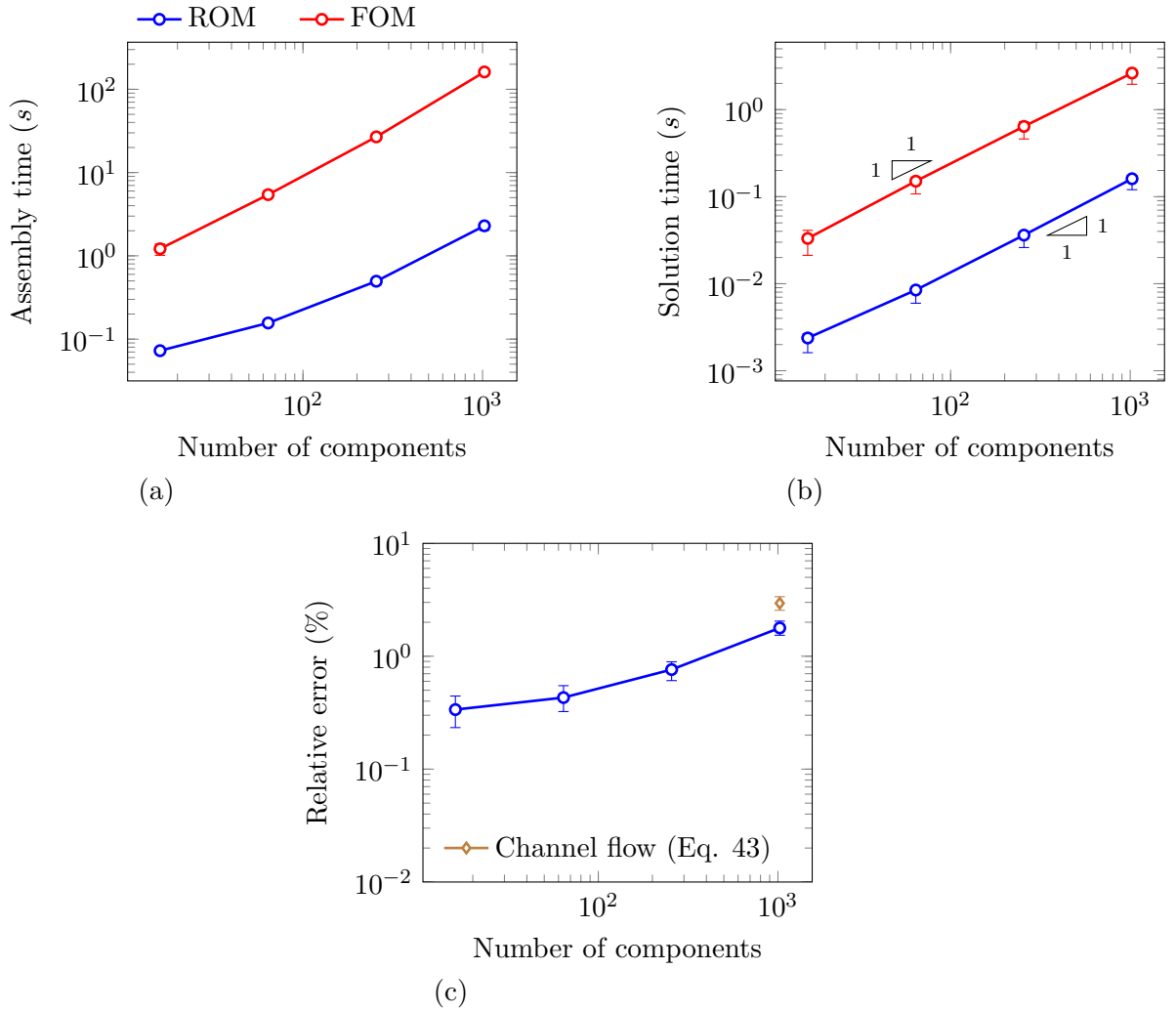


Figure 11: Performance of the ROM compared to the FOM for the Stokes flow equation, depending on the number of components  $M$ : (a) assembly time of the system; (b) computation time of the system; and (c) relative error of the ROM compared to the FOM solution. The marker denotes the median value of 100 test cases, and the error bar denotes 95%-confidence interval of the test cases.

Poisson equation, the variance between test cases is not large, slowly increasing with the size of the domain. This increasing error seems related to the extrapolative behavior emerging on a larger scale of domain. In example solutions in Figure 10, we observe that the flow tends to accumulate in the ‘empty’ components scattered in the domain, corresponding to the regions of least resistance, leading to absolute velocity much higher than the training data. The maximum velocity magnitude reaches up to  $\max(|\mathbf{u}|) \sim 10$ , which is an order of magnitude larger than the training range (41). Even for such a strongly extrapolative case, the ROM achieved a robust prediction with only a relative error of  $\sim 2\%$ .

Such robust ROM prediction is also made much faster compared to FOM. As shown in Figure 11 (a), the ROM accelerates the assembly time for  $M = 16$  about 10 times faster, and achieves a better scaling with  $M$ . Also, in Figure 11 (b), the computation time is reduced by a factor of 15 over all sizes of the domain.

In order to demonstrate robust prediction of ROM outside the training range, we also made ROM predictions on a channel flow boundary condition,

$$\mathbf{g}_{di} = \begin{cases} \left( U_{in} \left[ 1 - 4 \left( \frac{x_2}{N_c} - \frac{1}{2} \right)^2 \right], 0 \right) & \text{on } x_1 = 0, \\ \mathbf{0} & \text{on } x_2 = 0, N_c. \end{cases} \quad (43a)$$

Note that the samples generated with the flow-past-array problem (40) never have the no-slip wall condition on their outside boundaries ( ${}_s\partial\Omega_{di}$ ). This channel flow condition therefore poses a problem that is qualitatively different from the training data. Additionally, note that physically, the channel flow inlet boundary condition should occur at a slightly greater distance upstream, but this does not affect the present discussion. On the outflow direction boundary, the homogeneous Neumann boundary condition is applied,

$$\mathbf{g}_{ne} = \mathbf{0} \quad \text{on } x_1 = N_c. \quad (43b)$$

On the object surfaces inside the domain, no-slip wall boundary is set,

$$\mathbf{g}_{di} = \mathbf{0} \quad \text{on } \{ \mathbf{x} \in \partial\Omega(N_c) \mid x_1, x_2 \neq 0, N_c \}. \quad (43c)$$

A test predictive ROM solution is shown in Figure 10 (b). In Figure 11 (c), the global ROM constructed from the flow-past-array problem (40) made similarly robust predictions with relative error of  $\sim 3\%$ , only slightly larger

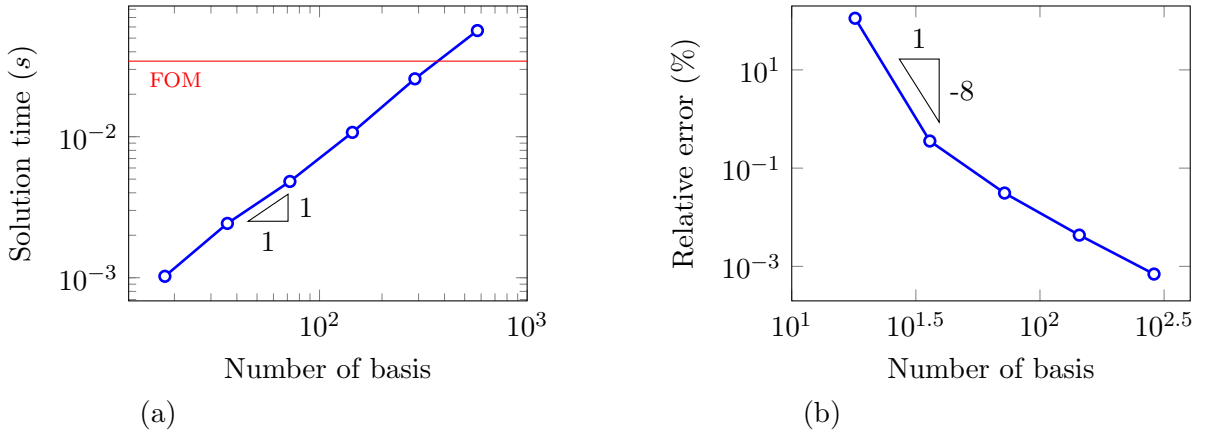


Figure 12: Performance of the component ROM for the Stokes flow equation: (a) solution time; and (b) relative error of the ROM solution. The solution time of the FOM is plotted (red) for reference.

than the case of (40). The assembly and solving time did not show a difference in this case. This demonstrates the robustness of the component ROM against general problems under the same physics.

#### 4.4.2. Performance scaling

As for the Poisson equation in Section 3.4.3, the performance scaling with the number of basis is investigated for the Stokes flow equation. The solution time and the relative error of the ROM are measured for the flow past array problem (40) on a random configuration of size  $\bar{\Omega}(4)$ . In Figure 12, similar to the Poisson equation, the accuracy of the ROM scales rapidly with the number of basis. With only  $R_r = 36$  basis, the ROM already achieves  $\sim 0.36\%$  relative error, while accelerating the solution time by a factor of 15. This again demonstrates the effectiveness of the ROM with the low-dimensional linear subspace. As for the Poisson equation, the scaling slows down as we increase  $R_r$ , following the singular value spectra in Figure 9(c).

## 5. Conclusion

In this work we address a common practical challenge in scaling up, where the data for the model reduction is provided only at small component-level

scales, and accurate prediction is required at a much larger scale. We developed a component ROM where the ROM is combined with DG-DD. The proposed method provides building blocks for robust and efficient prediction at an extrapolated scale.

The proposed method is demonstrated on two linear PDEs: the Poisson equation and the Stokes flow equation. For both cases, component ROM accelerates the solving time by a factor of  $15 \sim 40$ , for global domains up to 1000 times larger than the component domains. The resulting ROM was capable of robust prediction, with relative error of  $\sim 3\%$  over all scales, even for the problems that are qualitatively different from the samples used for the linear subspace training. The accuracy of the ROM scales with the linear subspace dimension  $R$  as  $\mathcal{O}(R^{-5})$  for Poisson and as  $\mathcal{O}(R^{-8})$  for Stokes. This is much faster than the  $\mathcal{O}(R)$  scaling of the corresponding solution time, enabling the computation to be both efficient and accurate with a low dimensional linear subspace.

Even for the ROM, of course, the computational cost scales with the size of the problem. Parallel computation of the ROM will be necessary for larger scale problems, particularly for three-dimensional simulations. Though not demonstrated here, our approach is not limited to the spatial dimension or the serial computing platform. Preconditioners for the component ROM, once developed, can achieve further acceleration at the larger scale problem. For positive-definite systems like the Poisson equation, two-level Schwarz preconditioners can be promising [27]. For indefinite systems like the Stokes flow equation, block preconditioners might need further factorization to maintain positive-definiteness.

It is well known that the linear subspace ROM cannot be naively applied to nonlinear problems. For polynomially nonlinear PDEs, such as the incompressible Navier–Stokes equation, the tensorial approach can be applied [30]. In other cases, hyper-reduction approaches are also available [31–33]. In all cases, similar component ROM variants can be formulated with the DG-DD, as all the model reduction techniques similarly exploit the physics equation.

## Acknowledgement

This work was performed under the auspices of the U.S. Department of Energy by Lawrence Livermore National Laboratory under contract DE-AC52-07NA27344 and was supported by Laboratory Directed Research and Development funding under project 22-SI-006. LLNL-JRNL-857774.

## References

- [1] R. Gross, R. Hanna, A. Gambhir, P. Heptonstall, J. Speirs, How long does innovation and commercialisation in the energy sectors take? historical case studies of the timescale from invention to widespread commercialisation in energy supply and end use technology, *Energy Policy* 123 (2018) 682–699. doi:<https://doi.org/10.1016/j.enpol.2018.08.061>. URL <https://www.sciencedirect.com/science/article/pii/S0301421518305901>
- [2] A. Toselli, *hp* discontinuous Galerkin approximations for the Stokes problem, *Mathematical Models and Methods in Applied Sciences* 12 (11) (2002) 1565–1597.
- [3] B. Cockburn, G. Kanschat, D. Schötzau, C. Schwab, Local discontinuous Galerkin methods for the Stokes system, *SIAM Journal on Numerical Analysis* 40 (1) (2002) 319–343.
- [4] G. J. Wagner, N. Moës, W. K. Liu, T. Belytschko, The extended finite element method for rigid particles in Stokes flow, *International Journal for Numerical Methods in Engineering* 51 (3) (2001) 293–313.
- [5] C. Pozrikidis, *Boundary integral and singularity methods for linearized viscous flow*, Cambridge university press, 1992.
- [6] R. K. Singh, Y. Fu, C. Zeng, P. Roy, J. Bao, Z. Xu, G. Panagakos, et al., Hydrodynamics of countercurrent flow in an additive-manufactured column with triply periodic minimal surfaces for carbon dioxide capture, *Chemical Engineering Journal* 450 (2022) 138124.
- [7] TIC – petra nova carbon capture project. URL <https://ticus.com/markets/power/coal-retrofit/petra-nova-carbon-capture-project/>
- [8] S. L. Brunton, J. L. Proctor, J. N. Kutz, Discovering governing equations from data by sparse identification of nonlinear dynamical systems, *Proceedings of the national academy of sciences* 113 (15) (2016) 3932–3937.

- [9] M. Raissi, P. Perdikaris, G. E. Karniadakis, Physics-informed neural networks: A deep learning framework for solving forward and inverse problems involving nonlinear partial differential equations, *Journal of Computational physics* 378 (2019) 686–707.
- [10] Z. Li, N. Kovachki, K. Azizzadenesheli, B. Liu, K. Bhattacharya, A. Stuart, A. Anandkumar, Fourier neural operator for parametric partial differential equations, arXiv preprint arXiv:2010.08895 (2020).
- [11] Y. Choi, K. Carlberg, Space–time least-squares Petrov–Galerkin projection for nonlinear model reduction, *SIAM Journal on Scientific Computing* 41 (1) (2019) A26–A58.
- [12] Y. Choi, P. Brown, W. Arrighi, R. Anderson, K. Huynh, Space–time reduced order model for large-scale linear dynamical systems with application to Boltzmann transport problems, *Journal of Computational Physics* 424 (2021) 109845.
- [13] Y. Choi, G. Boncoraglio, S. Anderson, D. Amsallem, C. Farhat, Gradient-based constrained optimization using a database of linear reduced-order models, *Journal of Computational Physics* 423 (2020) 109787.
- [14] D. M. Copeland, S. W. Cheung, K. Huynh, Y. Choi, Reduced order models for Lagrangian hydrodynamics, *Computer Methods in Applied Mechanics and Engineering* 388 (2022) 114259.
- [15] S. W. Cheung, Y. Choi, D. M. Copeland, K. Huynh, Local Lagrangian reduced-order modeling for the Rayleigh-Taylor instability by solution manifold decomposition, *Journal of Computational Physics* 472 (2023) 111655.
- [16] Y. Kim, Y. Choi, D. Widemann, T. Zohdi, A fast and accurate physics-informed neural network reduced order model with shallow masked autoencoder, *Journal of Computational Physics* 451 (2022) 110841.
- [17] K. Carlberg, Y. Choi, S. Sargsyan, Conservative model reduction for finite-volume models, *Journal of Computational Physics* 371 (2018) 280–314.

- [18] Y. Kim, K. Wang, Y. Choi, Efficient space–time reduced order model for linear dynamical systems in Python using less than 120 lines of code, *Mathematics* 9 (14) (2021) 1690.
- [19] S. McBane, Y. Choi, Component-wise reduced order model lattice-type structure design, *Computer methods in applied mechanics and engineering* 381 (2021) 113813.
- [20] S. McBane, Y. Choi, K. Willcox, Stress-constrained topology optimization of lattice-like structures using component-wise reduced order models, *Computer Methods in Applied Mechanics and Engineering* 400 (2022) 115525.
- [21] J. L. Eftang, A. T. Patera, A port-reduced static condensation reduced basis element method for large component-synthesized structures: approximation and a posteriori error estimation, *Advanced Modeling and Simulation in Engineering Sciences* 1 (1) (2014) 1–49.
- [22] D. B. P. Huynh, D. J. Knezevic, A. T. Patera, A static condensation reduced basis element method: approximation and a posteriori error estimation, *ESAIM: Mathematical Modelling and Numerical Analysis* 47 (1) (2013) 213–251.
- [23] K. Smetana, A new certification framework for the port reduced static condensation reduced basis element method, *Computer methods in applied mechanics and engineering* 283 (2015) 352–383.
- [24] S. Vallaghé, A. T. Patera, The static condensation reduced basis element method for a mixed-mean conjugate heat exchanger model, *SIAM Journal on Scientific Computing* 36 (3) (2014) B294–B320.
- [25] D. B. P. Huynh, D. J. Knezevic, A. T. Patera, A static condensation reduced basis element method: Complex problems, *Computer Methods in Applied Mechanics and Engineering* 259 (2013) 197–216.
- [26] P. Hansbo, Nitsche’s method for interface problems in computational mechanics, *GAMM-Mitteilungen* 28 (2) (2005) 183–206.
- [27] P. F. Antonietti, P. Pacciarini, A. Quarteroni, A discontinuous Galerkin reduced basis element method for elliptic problems, *ESAIM: Mathematical Modelling and Numerical Analysis-Modélisation Mathématique et Analyse Numérique* 50 (2) (2016) 337–360.

- [28] P. Pacciarini, P. Gervasio, A. Quarteroni, Spectral based discontinuous Galerkin reduced basis element method for parametrized Stokes problems, *Computers & Mathematics with Applications* 72 (8) (2016) 1977–1987.
- [29] M. Yano, Discontinuous Galerkin reduced basis empirical quadrature procedure for model reduction of parametrized nonlinear conservation laws, *Advances in Computational Mathematics* 45 (2019) 2287–2320.
- [30] T. Lassila, A. Manzoni, A. Quarteroni, G. Rozza, Model order reduction in fluid dynamics: challenges and perspectives, *Reduced Order Methods for modeling and computational reduction* (2014) 235–273.
- [31] K. Willcox, Unsteady flow sensing and estimation via the gappy proper orthogonal decomposition, *Computers & fluids* 35 (2) (2006) 208–226.
- [32] S. Chaturantabut, D. C. Sorensen, Nonlinear model reduction via discrete empirical interpolation, *SIAM Journal on Scientific Computing* 32 (5) (2010) 2737–2764.
- [33] M. Yano, A. T. Patera, An LP empirical quadrature procedure for reduced basis treatment of parametrized nonlinear PDEs, *Computer Methods in Applied Mechanics and Engineering* 344 (2019) 1104–1123.
- [34] J. T. Lauzon, S. W. Cheung, Y. Shin, Y. Choi, D. M. Copeland, K. Huynh, S-opt: A points selection algorithm for hyper-reduction in reduced order models, *arXiv preprint arXiv:2203.16494* (2022).
- [35] D. N. Arnold, An interior penalty finite element method with discontinuous elements, *SIAM journal on numerical analysis* 19 (4) (1982) 742–760.
- [36] C. Farhat, F.-X. Roux, A method of finite element tearing and interconnecting and its parallel solution algorithm, *International journal for numerical methods in engineering* 32 (6) (1991) 1205–1227.
- [37] C. Farhat, P.-S. Chen, J. Mandel, A scalable Lagrange multiplier based domain decomposition method for time-dependent problems, *International Journal for Numerical Methods in Engineering* 38 (22) (1995) 3831–3853.

- [38] C. Hoang, Y. Choi, K. Carlberg, Domain-decomposition least-squares Petrov–Galerkin (DD-LSPG) nonlinear model reduction, *Computer methods in applied mechanics and engineering* 384 (2021) 113997.
- [39] A. N. Diaz, Y. Choi, M. Heinkenschloss, A fast and accurate domain-decomposition nonlinear manifold reduced order model, *arXiv preprint arXiv:2305.15163* (2023).
- [40] A. Chatterjee, An introduction to the proper orthogonal decomposition, *Current science* (2000) 808–817.
- [41] Y. Liang, H. Lee, S. Lim, W. Lin, K. Lee, C. Wu, Proper orthogonal decomposition and its applications—part i: Theory, *Journal of Sound and vibration* 252 (3) (2002) 527–544.
- [42] C. W. Rowley, S. T. Dawson, Model reduction for flow analysis and control, *Annual Review of Fluid Mechanics* 49 (2017) 387–417.
- [43] R. Anderson, J. Andrej, A. Barker, J. Bramwell, J.-S. Camier, J. Cervený, V. Dobrev, Y. Dudouit, A. Fisher, T. Kolev, W. Pazner, M. Stowell, V. Tomov, I. Akkerman, J. Dahm, D. Medina, S. Zampini, MFEM: A modular finite element methods library, *Computers & Mathematics with Applications* 81 (2021) 42–74. doi:10.1016/j.camwa.2020.06.009.
- [44] Y. Choi, W. J. Arrighi, D. M. Copeland, R. W. Anderson, G. M. Oxberry, librom, [Computer Software] <https://doi.org/10.11578/dc.20190408.3> (oct 2019). doi:10.11578/dc.20190408.3. URL <https://doi.org/10.11578/dc.20190408.3>
- [45] Livermore Computing – Quartz.  
URL <https://hpc.llnl.gov/hardware/compute-platforms/quartz>
- [46] P. R. Amestoy, I. S. Duff, J.-Y. L’Excellent, J. Koster, A fully asynchronous multifrontal solver using distributed dynamic scheduling, *SIAM Journal on Matrix Analysis and Applications* 23 (1) (2001) 15–41.
- [47] P. R. Amestoy, A. Buttari, J.-Y. L’Excellent, T. Mary, Performance and scalability of the block low-rank multifrontal factorization on multicore architectures, *ACM Transactions on Mathematical Software (TOMS)* 45 (1) (2019) 1–26.

- [48] U. Trottenberg, C. W. Oosterlee, A. Schuller, *Multigrid*, Elsevier, 2000.
- [49] K. Stüben, A review of algebraic multigrid, *Numerical Analysis: Historical Developments in the 20th Century* (2001) 331–359.
- [50] D. Kay, D. Loghin, A. Wathen, A preconditioner for the steady-state Navier–Stokes equations, *SIAM Journal on Scientific Computing* 24 (1) (2002) 237–256.
- [51] H. C. Elman, D. J. Silvester, A. J. Wathen, *Finite elements and fast iterative solvers: with applications in incompressible fluid dynamics*, Oxford university press, 2014.
- [52] P. E. Farrell, L. Mitchell, F. Wechsung, An augmented Lagrangian preconditioner for the 3D stationary incompressible Navier–Stokes equations at high Reynolds number, *SIAM Journal on Scientific Computing* 41 (5) (2019) A3073–A3096.
- [53] C. Taylor, P. Hood, A numerical solution of the Navier-Stokes equations using the finite element technique, *Computers & Fluids* 1 (1) (1973) 73–100.
- [54] I. Babuška, Error-bounds for finite element method, *Numerische Mathematik* 16 (4) (1971) 322–333.
- [55] F. Brezzi, On the existence, uniqueness and approximation of saddle-point problems arising from Lagrangian multipliers, *Publications des séminaires de mathématiques et informatique de Rennes (S4)* (1974) 1–26.
- [56] O. Ladyzhenskaya, *The mathematical theory of incompressible viscous flows* (1963).